Computers in Biology and Medicine 149 (2022) 106049

Contents lists available at ScienceDirect

Computers in Biology and Medicine

journal homepage: www.elsevier.com/locate/compbiomed

Computational exploration of the dual role of the phytochemical fortunellin: Antiviral activities against SARS-CoV-2 and immunomodulatory abilities against the host

Shivangi Agrawal [a], Ekta Pathak [b,**], Rajeev Mishra [a,*], Vibha Mishra [a], Afifa Parveen [a], Sunil Kumar Mishra [c], Parameswarappa S. Byadgi [d], Sushil Kumar Dubey [d], Ashvanee Kumar Chaudhary [e], Vishwambhar Singh [f], Rameshwar Nath Chaurasia [g], Neelam Atri [h]

[a] *Bioinformatics, MMV, Institute of Science, Banaras Hindu University, India*
[b] *Institute of Diabetes and Obesity, Helmholtz Zentrum München, Neuherberg, Germany*
[c] *Department of Pharmaceutical Engineering & Technology, IIT (BHU), India*
[d] *Faculty of Ayurveda, Institute of Medical Sciences, Banaras Hindu University, India*
[e] *Department of Otorhinolaryngology, Institute of Medical Sciences, BHU, India*
[f] *Department of ENT, IMS, Banaras Hindu University, India*
[g] *Department of Neurology, Institute of Medical Sciences, Banaras Hindu University, India*
[h] *Department of Botany, MMV, Banaras Hindu University, India*

ARTICLE INFO

Keywords:
SARS-CoV-2
Fortunellin
Multi-target
Antiviral
Immunomodulation
Molecular dynamics simulation
MM-GBSA analysis
Enrichment analysis
Network pharmacology

ABSTRACT

Severe acute respiratory syndrome coronavirus-2 (SARS-CoV-2) infections generate approximately one million virions per day, and the majority of available antivirals are ineffective against it due to the virus's inherent genetic mutability. This necessitates the investigation of concurrent inhibition of multiple SARS-CoV-2 targets. We show that fortunellin (acacetin 7-O-neohesperidoside), a phytochemical, is a promising candidate for preventing and treating coronavirus disease (COVID-19) by targeting multiple key viral target proteins. Fortunellin supports protective immunity while inhibiting pro-inflammatory cytokines and apoptosis pathways and protecting against tissue damage. Fortunellin is a phytochemical found in Gojihwadi kwath, an Indian traditional Ayurvedic formulation with an antiviral activity that is effective in COVID-19 patients. The mechanistic action of its antiviral activity, however, is unknown. The current study comprehensively evaluates the potential therapeutic mechanisms of fortunellin in preventing and treating COVID-19. We have used molecular docking, molecular dynamics simulations, free-energy calculations, host target mining of fortunellin, gene ontology enrichment, pathway analyses, and protein-protein interaction analysis. We discovered that fortunellin reliably binds to key targets that are necessary for viral replication, growth, invasion, and infectivity including Nucleocapsid (N-CTD) (−54.62 kcal/mol), Replicase-monomer at NSP-8 binding site (−34.48 kcal/mol), Replicase-dimer interface (−31.29 kcal/mol), Helicase (−30.02 kcal/mol), Papain-like-protease (−28.12 kcal/mol), 2′-O-methyltransferase (−23.17 kcal/mol), Main-protease (−21.63 kcal/mol), Replicase-monomer at dimer interface (−22.04 kcal/mol), RNA-dependent-RNA-polymerase (−19.98 kcal/mol), Nucleocapsid-NTD (−16.92 kcal/mol), and Endoribonuclease (−16.81 kcal/mol). Furthermore, we identify and evaluate the potential human targets of fortunellin and its effect on the SARS-CoV-2 infected tissues, including normal-human-bronchial-epithelium (NHBE) and lung cells and organoids such as pancreatic, colon, liver, and cornea using a network pharmacology approach. Thus, our findings indicate that fortunellin has a dual role; multi-target antiviral activities against SARS-CoV-2 and immunomodulatory capabilities against the host.

---

* Corresponding author. Bioinformatics, MMV, Institute of Science, Banaras Hindu University, Varanasi, 221005, India.
** Corresponding author.,
E-mail addresses: ekta.pathak@helmholtz-muenchen.de, ektavpathak@gmail.com (E. Pathak), rajeev17@bhu.ac.in, mishrarajeev@gmail.com (R. Mishra).

https://doi.org/10.1016/j.compbiomed.2022.106049
Received 11 January 2022; Received in revised form 16 August 2022; Accepted 20 August 2022

1. Introduction

The coronavirus disease (COVID-19), caused by severe acute respiratory syndrome coronavirus-2 (SARS-CoV-2), has posed a serious threat to global public health. There had been 537,591,764 confirmed instances of COVID-19 documented as of June 22nd, 2022, resulting in 6,319,395 deaths globally [1]. COVID-19 patients exhibit respiratory symptoms, multi-organ failure, and inflammation, and therapeutic options are currently limited [2–4]. COVID-19 continues to spread over the world despite the availability of vaccines to the wider population, fueling the need for effective therapeutics to prevent and treat COVID-19 [5]. With various SARS-CoV-2 variations spreading internationally, there is concern about the vaccine's efficacy. Also, from patient to location, the effectiveness of repurposed drugs and vaccines differs [6,7]. The COVID-19 vaccines have been found to show reduced neutralization activities against the Omicron variant compared to the original and Delta variants of SARS-CoV-2 [8,9]. Although proposed drugs and vaccine candidates were approved for emergency treatment of COVID-19, the FDA recommended a few drugs to help control the pandemic. But there is still a need to expand the number of potential drug candidates that could have higher efficacy and fewer side effects for the treatment of COVID-19 [10–13].

Computational strategies are being extensively used to accelerate the discovery of low-cost and effective anti-SARS-CoV-2 potentials of phytocompounds against SARS-CoV-2 [14–21]. Several traditional herbal medicines have been reported as having inhibitory effects on SARS-CoV-2 infection in vitro and in vivo [20,22–24]. Many herbs have been shown to contain active antiviral natural components that effectively diminish COVID-19 virus transmission and disease progression [19,20,22], and some have been reported to work by targeting both (dual role) host and viral proteins [13,25]. However, understanding the mechanisms of action of antiviral compounds in herbal treatments could lead to more effective COVID-19 prevention and therapy.

SARS-CoV-2 is an enveloped virus with a 30 kb RNA genome that encodes four structural proteins: 16 non-structural proteins [26]. These proteins help the virus multiply and survive in the host cell [27]. So targeting several viral proteins is an appealing way to reduce viral load. The Main-protease (Mpro) is a crucial enzyme in SARS-CoV-2 replication and transcription [28,29]. Papain-like protease (PLpro) inhibits the activation of the host's innate immune responses, allowing the coronavirus to invade the host cell [30]. RNA-dependent RNA polymerase (RdRp) catalyzes the replication and transcription of the viral genome, making it essential for their survival [31]. The RNA processing enzyme uridine-specific endoribonuclease (NendoU) has been identified as critical for the viral life cycle [32]. Replicase of SARS-CoV-2 is vital for viral replication and transcription [33]. It undergoes dimerization, binds with RNA, interacts further with non-structural protein (NSP-8), and finally triggers the essential functions [34–36]. Helicase has both ATPase and helicase activity as it unwinds the RNA helices in an ATP-dependent manner [37]. Another promising target is 2′-O-methyltransferase. It participates in the cap formation at the 5′ ends of the viral RNA, which resembles the native mRNA of the host cells [38,39]. Inhibiting the multifunctional nucleocapsid protein can block both viral transcription and replication [40].

In this study, we have discovered a natural flavonoid O-glycoside compound, fortunellin (PubChem ID: 5317385), as a potent inhibitor of 11 domains of the eight key protein targets of SARS-CoV-2 using Molecular docking, MD simulations, and MM-GBSA analysis. Fortunellin, an antioxidant and anti-inflammatory compound found in Gojihwadi Kwath, an Indian traditional-Ayurvedic formulation, is also found in *Citrus japonica* var *margarita* fruits [41]. Gojihwadi Kwath is antiviral and helpful in COVID-19 management [42–45]. But its antiviral activity's molecular mechanism is unknown. Fortunellin inhibits Mpro dimerization [46]. Fortunellin also possesses antibacterial and anti-HIV-1 protease activities [47,48]. Fortunellin is non-toxic since it does not interact with the CYPs involved in drug metabolism. A molecule is considered prospective in early-stage drug research if it can reliably dock to the targeted protein with high binding affinity and dynamic stability [49–51]. Aiming to inhibit viral replication, growth, invasion, and infectivity, we tested the fortunellin binding to SARS CoV-2 key targets. We found that fortunellin targets the virus's Mpro, PLpro, RdRp, NendoU, Replicase monomer at the NSP-8 binding site, Replicase at the dimer interface, Replicase dimer, Helicase, 2′-O-ribose methyltransferase (MT), Nucleocapsid-NTD, and Nucleocapsid-CTD. Additionally, using free energy calculations and residue decomposition analysis, we show that fortunellin masks the catalytically important residues of these targets. In addition, we have used the network pharmacology approach to detect the impact of fortunellin on normal human bronchial epithelial cells (NHBE), lung cells, and organoids such as pancreatic, colon, liver, and cornea of the host system. We link the target host genes of fortunellin to anti-inflammatory, immunomodulatory, and apoptotic pathways. Our findings show that fortunellin has a dual role; multi-target antiviral activities against SARS-CoV-2 and immunomodulatory capabilities against the host. Given fortunellin's oral bioavailability and safety, this study could develop fortunellin as an orally active therapeutic against COVID-19 and new variants of coronavirus.

2. Methodology

2.1. Molecular docking of fortunellin to SARS CoV-2 key targets

The experimental structures of SARS-CoV-2 target proteins were retrieved from PDB [52] (Supplementary Table S1(A)). We used the dock prep tool [53] and refined the target proteins by adding missing atoms, polar hydrogen atoms, and Kollman charges to the residues and removing crystallographic water molecules. The structure of fortunellin (PubChem ID: 5317385) was retrieved from NCBI PubChem [54]. Energy minimization and geometry optimization of the structure were achieved using the Merck Molecular Force Field (MMFF94) in the Open Babel module of PyRx software [55]. Fortunellin was docked at the active binding pockets/functional sites of the SARS-CoV-2 protein targets employing a grid-based docking method using the rigid protein receptor and flexible ligand docking protocol. Molecular docking was achieved using the AutoDockVina 1.2.0 software [56,57] and SwissDock tools [58]. For the selected targets, the center grid box values and the number of grid points along the x, y, and z dimensions were set to cover the active/functional site and are given in Supplementary Table S1(C). The grid size was based on the target proteins' known active/functional site. The grid spacing was set to a default value of 1.0 Å. The exhaustiveness numbers 8 and 200 were used in the docking experiment (Supplementary Table S1(B)). The structures were visualized and analyzed using UCSF Chimera 1.15 [53].

2.2. Molecular dynamics (MD) simulation of fortunellin-SARS CoV-2 key target complex

To validate the stability of the docked complex of fortunellin with Mpro, PLpro, RdRp, Endoribonuclease, Replicase (monomer as well as a dimer), Helicase, Methyltransferase, Nucleocapsid NTD, and N-CTD were subjected to molecular dynamics simulation for a timescale of 200 ns (ns) using GROMACS 2021.1 [59] and CHARMM 36 m force field parameter set [60]. The web server SwissParam was used to generate the ligand topologies as well as the atomic charges of the ligands [61]. We have ignored the entropy contribution in the binding energy calculation. Because of the high computational cost and limited prediction accuracy of NMA, many applications using MM/GBSA and MM/PBSA ignore the entropy change for protein-ligand binding. The MD simulations were conducted in a cubic water box solvated with TIP3P water molecules. Periodic boundary conditions were imposed in all directions, and Na^+ Cl^- counter ions were added to make the system electrically neutral. The energy minimization of the systems was then achieved through 50,000 steps of steepest descents to alleviate any steric conflicts. After that, energy minimization for 100 ps was followed by NVT and NPT equilibration. These systems were then submitted to MD simulation at 300 K for 200 ns, with no restrictions on the residues, after they had been equilibrated in terms of pressure and density. Using a Berendsen thermostat, the system's temperature was kept at 300 K throughout the experiment. The particle mesh Ewald method [62] was employed to account for the long-range electrostatic interactions, and the LINCS algorithm [63] was used, with a time step of 2fs to restrain bond lengths. The constant temperature and pressure (300 K and 1 bar) were maintained using a V-rescale thermostat [64] and Parrinello-Rahmanbarostat [65]. The production run was performed for 200 ns with a leapfrog integrator [66], and the coordinates were saved every 10 ps. A total of 20,000 frames were generated. MD trajectories were analyzed using the RMSD (root mean square deviation), RMSF (root mean square fluctuation), Rg (radius of gyration), hydrogen bond, and minimum distance between the ligand (as one group) and the protein target (another group). The tools of GROMACS 2021.1 were utilized [59]. The plots were generated using XMGRACE [67]. To analyze the target-fortunellin interactions, we used the representative snapshot of the most populated cluster obtained from the 150–200 ns simulations using MD movie analysis of UCSF Chimera [53] package, and 2D interaction profiling was constructed using Maestro-12.4 (Schrödinger Release 2020–2: Maestro, Schrödinger, LLC, New York, NY, USA).

2.3. *Binding free energy calculations of the SARS-CoV-2 targets and fortunellin complexes*

We have performed the MD in GROMACS 2021.1, and the MMGBSA analysis was calculated using the MMPBSA.py program of AmberTools21 (AMBER2021) [68–70]. We have used VMD 1.9.3 [71] to convert the trajectory generated by GROMACS program to the AMBER compatible trajectory. We have used the GROMBER tool of AMBER2021 and converted the GROMACS topology file to AMBER topology file. The GB radius was set to mbondi2. We generated complex, receptor, and ligand topology files from a solvated topology file using the ante-MMPBSA.py.

For free energy calculation, the following equation was used:

$$\Delta G\ (\text{bind}) = \Delta G\ (\text{complex}) - [\Delta G\ (\text{receptor}) + \Delta G\ (\text{ligand})]$$

The binding free energy (ΔTotal) was estimated using van der Waals energy (ΔE_{VDW}); electrostatic energy (ΔE_{EEL}); polar solvation energy (ΔE_{GB}); non-polar solvation energy (ΔE_{Surf}); total solvation free energy (ΔG_{Sol}); total gas-phase free energy (ΔG_{gas}). From the 200 ns MD simulation run, a total of 1000 snapshots were extracted, starting from the frame 15000 to 20000 with an interval of 5 snapshots. Furthermore, we also performed a per-residues energy decomposition analysis to evaluate the energy contribution of each residue to the total energy.

2.4. *Assessment of pharmacokinetic and pharmacodynamics features*

Using ADMETlab 2.0 [72] and pkCSM servers [73], the comparative pharmacokinetic attributes like absorption, distribution, metabolism, excretion (ADME), and other important pharmacological properties (physicochemical properties, lipophilicity, water-solubility, and drug-likeness) of fortunellin were calculated. Furthermore, toxicity parameters like mutagenicity (AMES mutagenesis), hepatotoxicity, cytotoxicity, minnow toxicity, etc., of fortunellin were also predicted.

2.5. *Prediction of upregulated host gene targets of fortunellin in COVID-19 infected cells/organoids*

We predicted the targets of fortunellin using the similarity ensemble approach [74] and the SwissTargetPrediction tool [75]. Next, the differentially expressed (DE) gene lists specific to human cells/tissues/organoids, including human NHBE cells (GSE147507), lung cells (GSE147507), pancreatic organoids (GSE151803), colon organoids (GSE148696), liver organoids (GSE151803), and cornea organoids (GSE164073) were downloaded from the Enrichr library "COVID-19_Related_Gene_Sets_2021". Using Venn diagram (http://bioinfogp.cnb.csic.es/tools/venny/), we identified the tissue-specific gene targets of fortunellin, which were upregulated after infection with COVID-19.

2.6. *Functional enrichment analysis*

The identified host gene targets of fortunellin were further analyzed for its enriched biological processes, molecular functions, and cellular components utilizing the Enrichr tool [76]. Scatter plots were generated using the ggplot2 in Rstudio [77]. To obtain statistically significant results, we used the cut-off p-value of less than 0.05 (p-value <0.05).

2.7. *Protein-protein interaction analysis, module detection, and pathway analysis*

Furthermore, the Cytoscape STRING App plugin [78] was used to investigate the protein-protein interaction network of fortunellin's target genes. With a confidence score of 0.4, we added 100 neighbor genes to the network. The expression of the integrated genes was investigated for its upregulation in COVID-19 infected cells/organoids using Enrichr library "COVID-19_Related_Gene_Sets_2021. We identified the network module using Cytoscape's MCODE plugin [78]. MCODE detects clusters that are highly interconnected within a network. Furthermore, we used Cytoscape'scytohubba plugin's [79] maximum clique centrality (MCC) approach to determine the important (HUB) genes that were also targeted by fortunellin. Finally, we used the KEGG database [80] to identify the top five metabolic pathways of these modules to ascertain fortunellin's mode of action in the corresponding cell/organoids.

3. Results

3.1. *Fortunellin targets 11 active pockets of eight key target proteins of SARS-CoV-2*

We have found that fortunellin, a phytochemical derived from the ayurvedic (Indian traditional medicine) formulation Gojihwadi, has multitargeting potential against SARS-CoV-2. Fortunellin showed a reliable negative binding energy, better than the reference ligand (Supplementary Table S1(B)), against the 11 ligand binding sites of eight key protein targets, including the virus's main protease (−8.9 kcal/mol), papain-like protease (−8.7 kcal/mol), RdRp (−9.2 kcal/mol), NendoU (−9.0 kcal/mol), replicase monomer at NSP-8 binding site (−8.6 kcal/mol), replicase monomer at dimeric interface (−7.0 kcal/mol), replicase dimer (−8.2 kcal/mol), helicase (−9.8 kcal/mol), 2′-O-methyltransferase (−9.4 kcal/mol), nucleocapsid-NTD (−8.0 kcal/mol), and nucleocapsid-CTD (−9.2 kcal/mol) (Fig. 1, Supplementary Table S1(B)). The docking experiment was carried out with the exhaustiveness numbers of 8 and 200. The docked complex's structural superimposition showed that the binding mode of the ligand with exhaustiveness numbers of 8 and 200 was comparable (Supplementary Figure S1 and Supplementary Table S1(B)). The molecular interactions of the fortunellin-target protein docked complexes are given in Supplementary Table S2. Furthermore, to evaluate the reliability and validate the stability of docked complexes, each of the 11 fortunellin-SARS-CoV-2 target complexes was subjected to a 200 ns MD simulation, producing a total of 2.2 μs of molecular trajectory data for analysis.

3.2. *Molecular dynamics simulation and MMGBSA analysis of fortunellin-Mpro complex*

We observed a stable backbone conformational state with an average

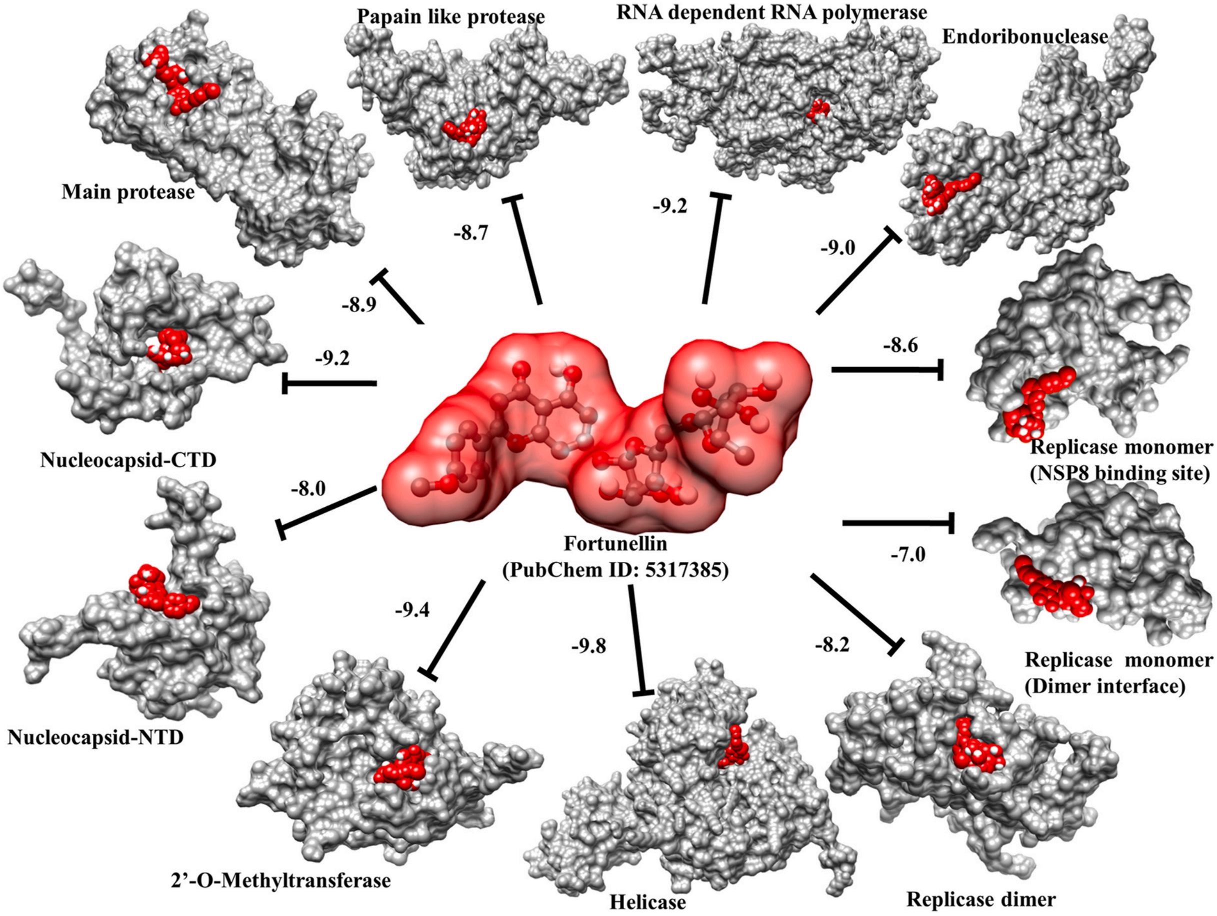

Fig. 1. Molecular docking of fortunellin to SARS CoV-2 targets. SARS-CoV-2 protein targets are depicted in a grey surface view. Fortunellin is shown as a red color surface. The binding energy values (kcal/mol) are calculated using AutodockVina 1.2.0 [56].

RMSD value of 0.24 ± 0.06 nm (Fig. 2(I-A)), suggesting interaction stability. A steady Rg value ranging between 2.22 and 2.28 nm indicated a compact and stable structure (Fig. 2(I–B)). A minimum distance of ~0.28 nm between the fortunellin (as one group) and the protein target (another group) indicated a stable interaction (Fig. 2(I–C)). The minimum distance ensures that the ligand is in the target's pocket. RMSF analysis revealed that the catalytic dyad, His41-Cys145 residues, was stably masked by the fortunellin (Fig. 2(I-D)). Fortunellin-Mpro complex exhibited an average of three hydrogen bonds (Fig. 2(I-E)). The 2D interactions analysis revealed that fortunellin interacts with the catalytic dyad residues His41 and Cys145. Also, the formation of two H-bond pairs with Cys145 and Glu166, charged interactions, and hydrophobic and hydrophilic interactions provide extra stability to the complex (Fig. 2(I–F)). Thus, it marks the unavailability of the main protease for participating in polyprotein cleavage [81,82]. Furthermore, MMGBSA analysis showed a reliable binding free energy of −21.6386 kcal/mol (Table 1). As shown in Fig. 2(I-G), residue decomposition analyses revealed the key residues, including Thr25, His41, Cys145, Met149, Met 165, and Gln189, stabilizing the fortunellin-Mpro complex.

3.3. MD simulation and MMGBSA analysis of fortunellin papain-like protease complex

Fortunellin-PLpro complex was stabilized with an average RMSD value of 0.23 nm (Fig. 2(II-A)). A steady Rg value of ~2.52 nm suggested compactness and stability (Fig. 2(II–B)). Fortunellin-PLpro complex was stabilized at a minimum distance of ~0.20 nm (Fig. 2(II–C)). RMSF analysis of active site residues, especially the catalytic triad residues Cys111-His272-Asp286 of PLpro revealed low fluctuations and indicated a stable complex formation (Fig. 2(II-D)). The stability is contributed by three to four H-bonds (Fig. 2(II-E)). The 2D interaction analysis revealed that fortunellin was stabilized by H-bonds contributed by Gln250, Gly266 backbone; non-polar and polar interactions. Notably, interaction with His272, one of the catalytic triad residues, suggests its inhibitory role (Fig. 2(II–F)). Furthermore, MMGBSA analysis revealed a reliable binding free energy of −28.1218 kcal/mol (Table 1). Residue decomposition analyses revealed that the Pro248, Tyr264, Tyr268, and Cys270 residues majorly contributed to the total binding energy favoring the PLpro-fortunellin complex formation (Fig. 2(II-G)).

3.4. MD simulation and MMGBSA analysis of fortunellin-RdRp complex

In the fortunellin-RdRp complex, the stability and tight packing of the ligand-target complex were validated by a stable RMSD profile (0.45 nm) (Fig. 2(III-A)), and Rg values of 3.27 nm (Fig. 2(III–B)), respectively. The ligand and target were stabilized at a minimum distance of 0.16–0.22 nm (Fig. 2 (III–C)). The RMSF analysis (Fig. 2(III-D)) revealed that catalytic residues ^{759}SDD^{761} and the divalent-cation-binding residue D618 for RdRp were stabilized. An average of two to three H-bonds showed the stability of the complex (Fig. 2(III-E)). 2D interaction analysis revealed the residues stabilizing the complex. Extra stability is provided by the formation of an H-bond with the backbone of Ala550, Ile548, and Arg555 (Fig. 2(III–F)). MMGBSA analysis revealed free binding energy of −19.9824 kcal/mol (Table 1). The residues Ala547, Ile548, Ser549, Ala550, Lys551, Asn552, Arg555, and Lys798 contributed to the favorable energy in the fortunellin-RdRp complex stabilization (Fig. 2(III-G)). Thus, targeting the RdRp active sites with fortunellin could be a potential therapeutic option.

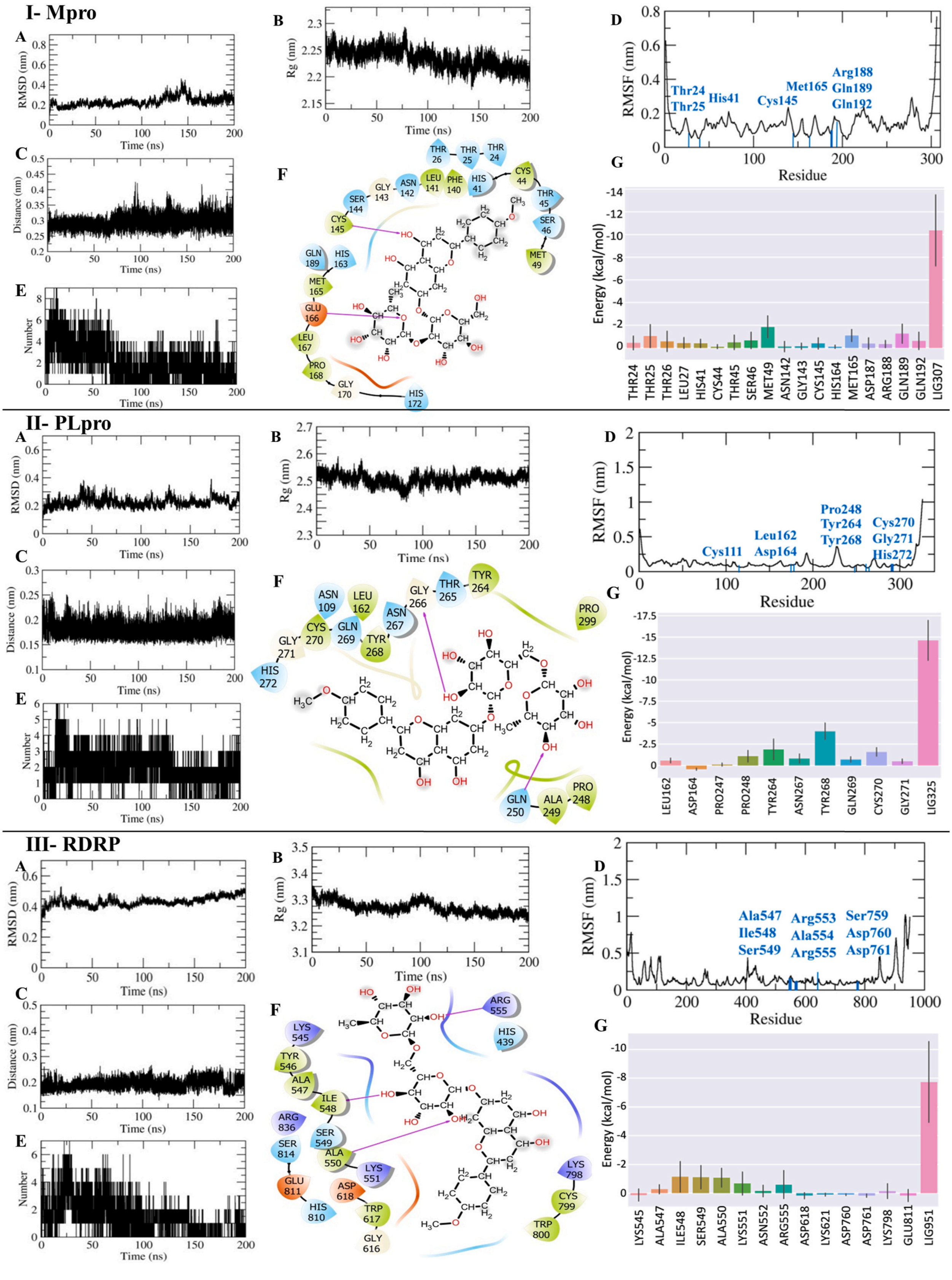

Fig. 2. MD analysis of fortunellin-SARS-CoV-2 complex. I) Mpro, II) PLpro, III) RdRp in the complex. The plots are (A) RMSD trends for the backbone of SARS-CoV-2 targets (B) Radius of gyration (C) minimum distance between the ligand (as one group) and the protein target (another group) (D) RMSF (E) distribution of H-bonds, (F) 2D-interaction of target-fortunellin complex (G) residue wise contribution to the binding energy of the complex.

Table 1

Binding free energy components of major protein targets of SARS CoV-2 with fortunellin calculated by MM-GBSA analysis.

SARS CoV-2 Targets	ΔE_{VDW}	ΔE_{EEL}	ΔE_{GB}	ΔE_{SURF}	ΔG_{gas}	ΔG_{Sol}	ΔTotal
Main protease (Mpro)	−34.6921 ± 8.1008	−8.2224 ± 5.5123	25.8394 ± 6.2532	−4.5636 ± 0.9617	−42.9145 ± 10.9054	21.2758 ± 5.5307	**−21.6386** ± 6.7620
Papain like protease (PLpro)	−37.3163 ± 3.8958	−17.9992 ± 5.7697	31.6529 ± 4.3466	−4.4593 ± 0.3950	−55.3154 ± 7.2522	27.1936 ± 4.1915	**−28.1218** ± 4.3684
RNA dependent RNA polymerase (RdRp)	−30.5246 ± 4.5811	−11.4507 ± 11.5929	26.0611 ± 9.3520	−4.0683 ± 0.4998	−41.9753 ± 11.3421	21.9929 ± 9.2557	**−19.9824** ± 3.9152
Endo-ribo nuclease (NendoU)	−24.8025 ± 4.3057	−5.5534 ± 10.4810	16.5303 ± 8.7225	−2.9866 ± 0.5737	−30.3559 ± 11.4113	13.5437 ± 8.5521	**−16.8122** ± 4.6891
Replicase (monomer)- NSP-8 binding site	−45.3806 ± 4.2238	−12.6115 ± 6.5500	29.5393 ± 4.6927	−6.0315 ± 0.4546	−57.9920 ± 8.0942	23.5077 ± 4.4838	**−34.4843** ± 5.0140
Replicase (monomer) dimer interface	−33.9562 ± 5.9479	−5.4207 ± 6.2276	21.7849 ± 7.1180	−4.4565 ± 0.7615	−39.3768 ± 10.5510	17.3285 ± 6.5329	**−22.0484** ± 4.9459
Replicase (dimer)	−43.9169 ± 6.2230	−29.3451 ± 14.5247	47.8652 ± 11.9748	−5.8939 ± 0.8274	−73.2620 ± 18.1369	41.9713 ± 11.3507	**−31.2907** ± 8.2294
Helicase	−48.8710 ± 4.7475	−37.7330 ± 10.4724	63.4362 ± 8.2675	−6.8620 ± 0.6780	−86.6040 ± 12.1651	56.5742 ± 7.8932	**−30.0298** ± 6.0144
2′-O-methyltransferase	−37.2238 ± 5.9696	−13.1796 ± 11.7826	32.2444 ± 9.9715	−5.0129 ± 0.8717	−50.4034 ± 14.3369	27.2315 ± 9.4562	**−23.1719** ± 6.5122
Nucleocapsid (N-NTD)	−31.0888 ± 6.6578	−15.8757 ± 9.7707	34.5686 ± 9.9877	−4.5284 ± 0.9410	−46.9645 ± 12.7222	30.0401 ± 9.4599	**−16.9243** ± 5.3302
Nucleocapsid (N-CTD)	−59.6115 ± 4.5382	−25.9493 ± 11.6046	38.6931 ± 7.4143	−7.7539 ± 0.4125	−85.5609 ± 10.1257	30.9392 ± 7.5381	**−54.6217** ± 5.0680

All energies are in kcal/mol along with their standard deviation. ΔE_{VDW}*, van der Waals energy;* ΔE_{EEL}*, Electrostatic energy;* ΔE_{GB} *Polar solvation energy;* ΔE_{Surf}*, Non-polar solvation energy;* ΔG_{Sol}*, Total solvation free energy;* ΔG_{gas}*, Total gas-phase free energy and* $\Delta Total$*, is the binding free energy.*

3.5. MD and MMGBSA analysis of fortunellin-endoribonuclease (NendoU) complex

Fortunellin-endoribonuclease complex was stabilized with an RMSD between 0.4 and 0.6 nm (Fig. 3 (I-A)) and was also compact (Rg value of 2.5–2.7 nm) (Fig. 3 (I–B)). Fortunellin at a minimum distance of 0.2 nm with endoribonuclease suggested its proximity (Fig. 3 (I–C)). A stable RMSF profile of binding site residues His235, His250, Lys290, Ser294, Thr341, and Tyr343 suggests the thermodynamic stability of the endoribonuclease-fortunellin complex (Fig. 3 (I-D)). An average of three H-bonds between target-ligand was observed (Fig. 3 (I-E)). Fortunellin was bound to endo-ribonuclease enzyme utilizing the polar amino acids His235, Ser316, and Thr341; hydrophobic Val314, Val315, Met 331, Trp333, Cys334, and Tyr343, and charged Lys335, Asp336, and Glu340 amino acids respectively. An additional H-bond with Cys334 and Glu340 contributed to its stability (Fig. 3 (I–F)). Furthermore, the binding free energy calculations using the MMGBSA revealed reliable binding free energy of −16.8122 kcal/mol (Table 1). Trp333 and Cys334 residues majorly contributed to the binding energy. In addition, Lys290, Met331, Cys334, Glu340, Thr341and Tyr343 with negative binding energy suggest the favorable fortunellin-endoribonuclease complex formation (Fig. 3 (I-G)).

3.6. MD simulation and MMGBSA analysis of fortunellin-replicase (monomer) at the NSP-8 binding site and the dimer interface

Fortunellin was found to bind at two sites, equally important in viral replication, i.e., the NSP-8 binding site [83] as well as the dimeric interface of the replicase enzyme. Firstly, the NSP-8 binding site of the replicase-fortunellin complex was investigated. The complex showed a stabilized RMSD value of 0.59 nm up to 125 ns, after which RMSD was stabilized at a lower value of 0.25 nm (Fig. 3(II-A)). The Rg value was stabilized at ~1.5 nm (Fig. 3(II–B)). The distance between the ligand and receptor was maintained at an average value of 0.2 nm (Fig. 3 (II–C)). The RMSF values of all the interacting residues, including Leu46, Cys74, Arg75, Phe76, Lys87, Leu89, Phe91, Val111, and Leu113, were found to be ~0.1 nm (Fig. 3(II-D)). The ligand-receptor, on average, consists of two to three H-bonds (Fig. 3(II-E)). 2D-interaction analysis revealed hydrogen bonded interactions with the backbone of Leu10 and Thr110; and other polar and non-polar interactions (Fig. 3(II–F)). Using MMGBSA analysis, we found binding energy of −34.4843 kcal/mol (Table 1), favouring ligand-receptor interactions. Furthermore, the residue-wise energy decomposition revealed that Gln12, Leu30, Tyr32, Leu46, Phe76, Thr78, Lys87, Leu107, Thr110, Val111, and Leu113 are the residues contributing to the binding energy (Fig. 3 (II-G)).

Next, we explored the fortunellin binding at the functionally important dimeric interface of the replicase. An RMSD of 0.25–0.33 nm (Fig. 3(III-A)) showed that the complex was stable and compact. After 100 ns, we observed a conformational change in the protein complex, but fortunellin was still found to reside in the pocket of replicase. The Rg value of 1.42 nm (Fig. 3(III–B)) was observed, and the minimum distance between ligand and receptor was maintained at 0.2 nm (Fig. 3 (III–C)) throughout the 200 ns simulation run. The RMSF of the GXXXG domain responsible for dimer formation was observed to be stabilized upon ligand binding at 0.2 nm (Fig. 3(III-D)). Complex showed two to seven H-bonds (Fig. 3 (III-E)). 2D-interaction analysis revealed that fortunellin was stabilized at dimeric interface contributed by GxxxG domain residues: Gly101, Met102, Leu104, and Gly105. It showed interactions with polar, non-polar, and charged amino acids including one hydrogen bond interaction with residues Asn97 (Fig. 3(III–F)). MMGBSA study estimated the overall binding free energy to be −22.0484 kcal/mol (Table 1). Met1, Asn2, Asn3, Pro7, Val8, Leu98, Arg100, Gly101, Met102, Val103, Leu104, Gly105, and Ala108 also contributed to the observed binding energy (Fig. 3(III-G)). Thus, occupying the enzyme's interface may prevent dimer formation, which in turn may hamper the NSP8 binding.

3.7. MD simulation and MMGBSA analysis of fortunellin-replicase (dimer) complex

We also investigated the binding and stability of fortunellin at the pocket formed after replicase dimerization. A steady RMSD value of 0.30 ± 0.08 nm (Fig. 4(I-A)) and a stable Rg value of ~2.0 nm (Fig. 4(I–B)) indicated the stability and compactness of the complex. The minimum distance analysis showed that fortunellin was stabilized at a ~0.19 nm distance from the protein (Fig. 4(I–C)). The binding site residues, including Gly101, Met102, Val103, Leu104, Gly105, and Leu46, showed stabilized RMSF (Fig. 4(I-D)). We observed around five to six H-bonds contributing to the stability of the complex (Fig. 4(I-E)). These H-bonds were contributed by Asn2 of chain A, Arg75 (3 H-bonds), and Gly83 of

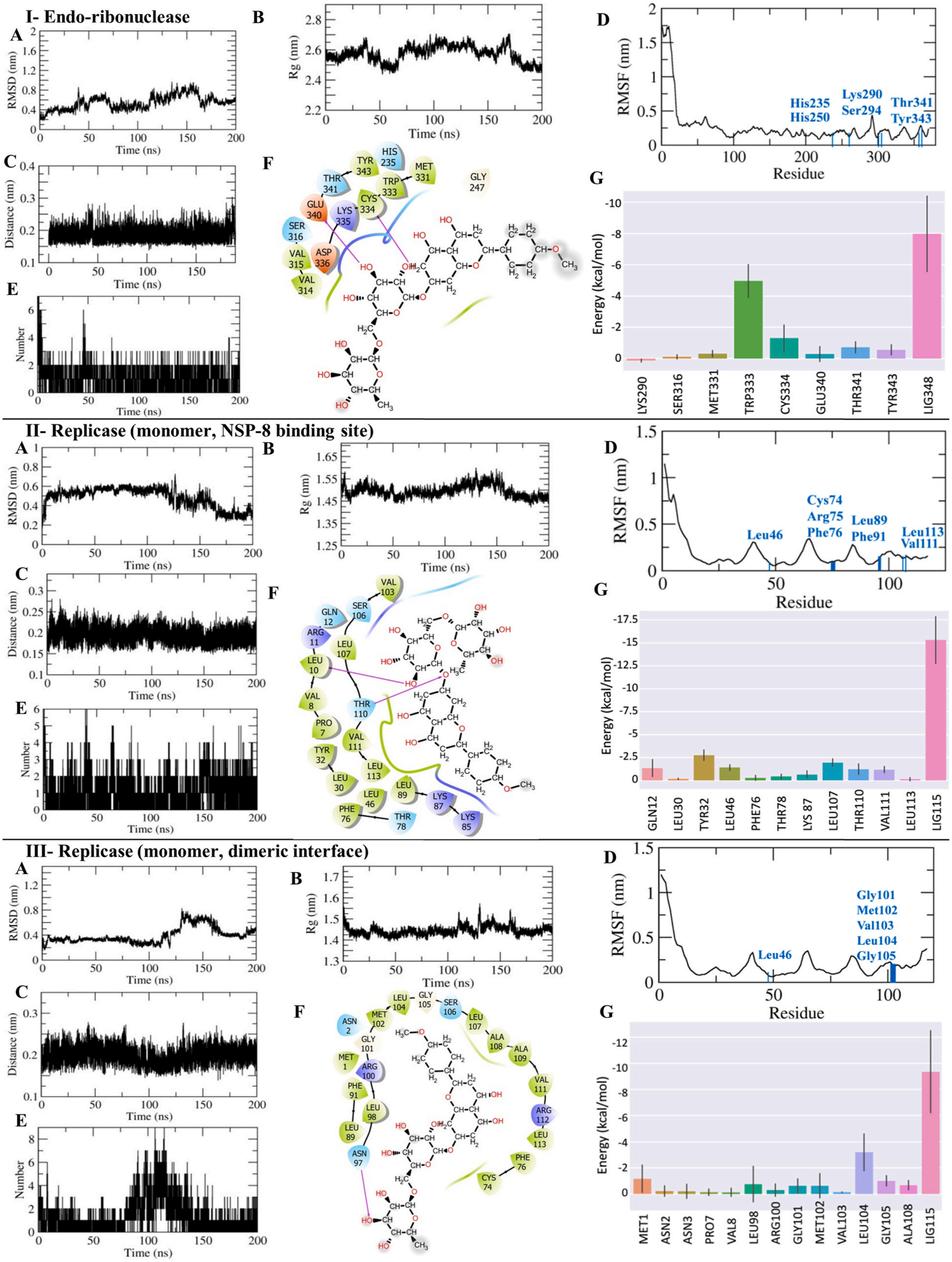

Fig. 3. MD analysis of fortunellin-SARS-CoV-2 complex. I) NendoU, II) Replicase monomer at NSP-8 site, III) Replicase monomer at dimer-interface. (A) RMSD trends for the backbone of SARS-CoV-2 targets, (B) Radius of gyration, (C) minimum distance between the ligand (as one group) and the protein target (another group), (D) RMSF (E) distribution of H-bonds, (F) 2D-interaction of target-fortunellin complex (G) residue wise contribution to the binding energy of the complex.

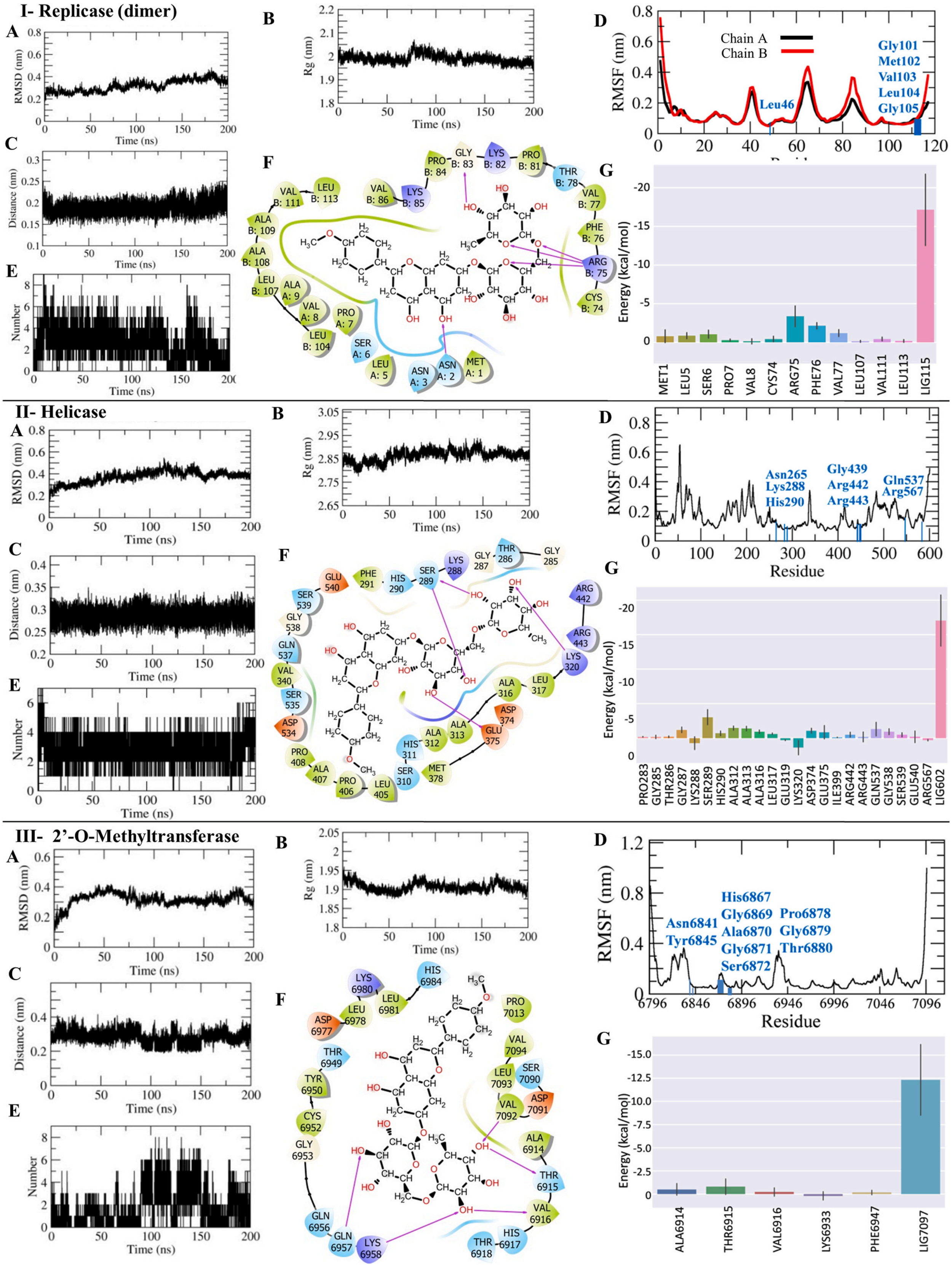

Fig. 4. MD analysis of fortunellin-SARS-CoV-2 complex. I) Replicase dimer, II) Helicase, III) 2′-O-Methyltransferase. The plots are (A) RMSD trends for the backbone of SARS-CoV-2 targets, (B) Radius of gyration, (C) minimum distance between the ligand (as one group) and the protein target (another group), (D) RMSF (E) distribution of H-bonds (F) 2D-interaction of target-fortunellin complex (G) residue wise contribution to the binding energy of the complex.

chain B (Fig. 4 (I–F)). MMGBSA analysis of fortunellin-replicase (dimer) complex yielded an overall binding free energy of −31.2907 kcal/mol (Table 1). As shown in (Fig. 4(I-G)), residues of both the chains contributed to the negative free energy, including Met1, Leu5, Ser6, Pro7, and Val8 residues of Chain A and Cys74, Arg75, Phe76, Val77, Leu107, Val111 and Leu113 residues of Chain B, respectively. Thus, fortunellin binding to the cavity at the dimeric contact point of replicase may prevent it from binding with RNA and NSP-8 essential for viral propagation.

3.8. MD simulation and MMGBSA analysis of fortunellin-helicase complex

The structural stability of the fortunellin-helicase complex was assessed with an RMSD value of ~0.4 nm (Fig. 4 (II-A)). A steady Rg value of ~2.85 nm ensured the compactness of the complex (Fig. 4 (II–B)). The minimum distance between fortunellin and helicase was stabilized at ~0.27 nm and maintained until the simulation end (Fig. 4 (II–C)). The RMSF value for residues including Asn265, Lys288, His290, Gly439, Arg442, Arg443, Gln537, and Arg567 was found to be low, suggesting the stability of the complex (Fig. 4(II-D)). We found that four H-bonds were contributing to the stability of the complex (Fig. 4(II-E)).

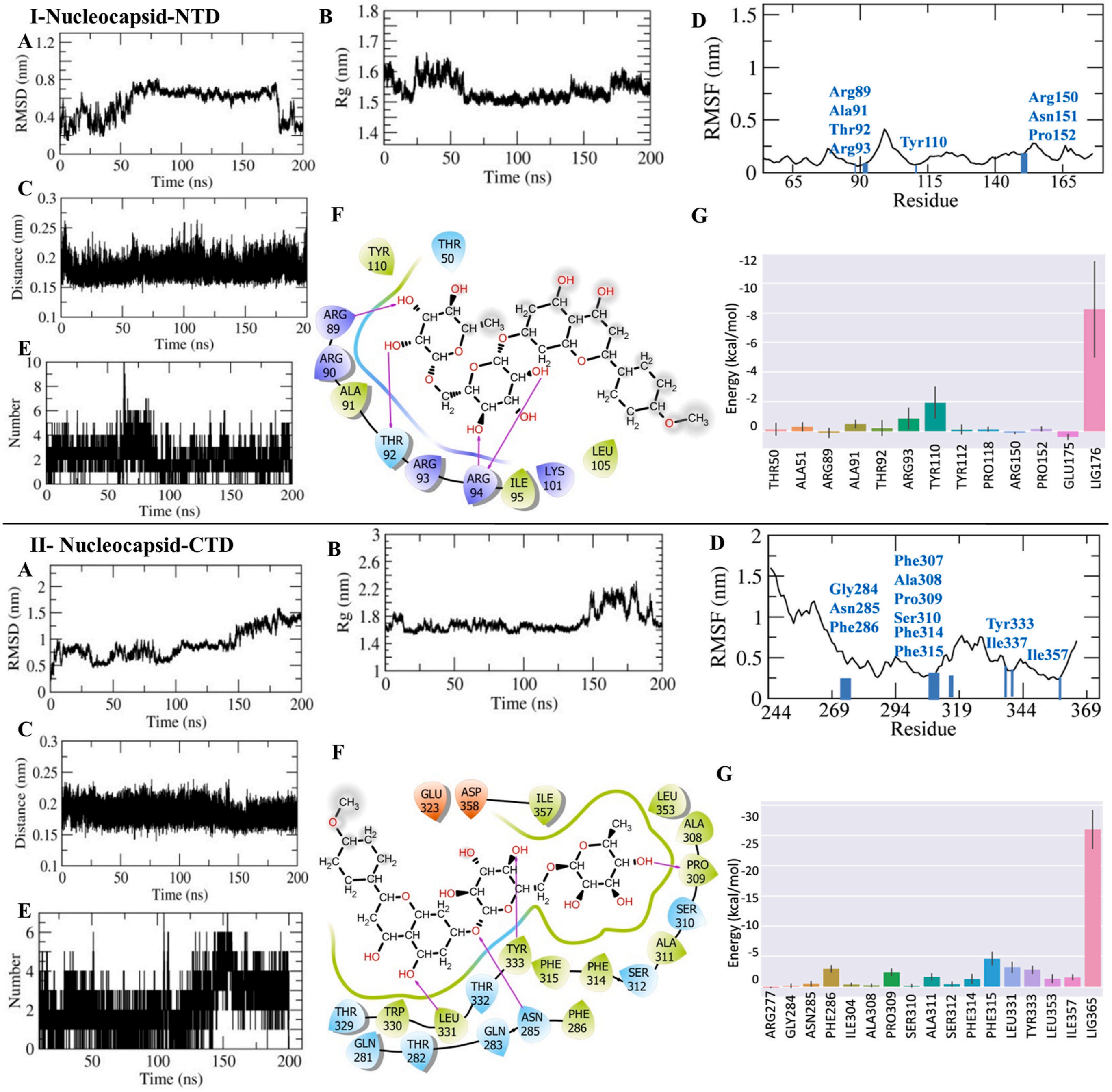

Fig. 5. MD analysis of fortunellin-SARS-CoV-2 complex. I) Nucleocapsid (N-NTD) and II) Nucleocapsid (C-NTD). The plots are (A) RMSD trends for the backbone of SARS-CoV-2 targets (B) Radius of gyration (C) minimum distance between the ligand (as one group) and the protein target (another group) (D) RMSF (E) distribution of H-bonds, (F) 2D-interaction of target-fortunellin complex (G) residue wise contribution to the binding energy of the complex.

These H-bonds were contributed by Ser289 (two H-bonds), Lys320, and Glu375 (Fig. 4 (II–F)). Notably, interactions with catalytically and functionally important residues Lys288, His290, and Arg443 enabled masking of the pocket and thus, making them unavailable during the viral replication process (Fig. 4(II–F)). Using MMGBSA, the total binding free energy was observed to be −30.0298 kcal/mol (Table 1). The catalytically important residues His290, Arg442, and Arg443, contributed to the binding free energy. Also, Pro283, Gly285, Thr286, Gly287, Ser289, Ala312, Ala313, Ala316, Leu317, Asp374, Glu375, Ile399, Gln537, Gly538, Ser539, and Glu540 were found to be contributing toward the negative binding free energy Fig. 4(II-G)).

3.9. MD simulation and MMGBSA analysis of fortunellin-2′O methyltransferase complex

Fortunellin-methyltransferase complex showed a stable and compact structure with a steady RMSD of 0.36 ± 0.03 nm (Fig. 4 (III-A)) and an Rg value of 1.91 ± 0.03 nm (Fig. 4(III–B)). The minimum distance of 0.22 nm (Fig. 4 (III–C)) further suggested the formation of a stable complex. A stable RMSF value for the catalytically important residues at the binding site further suggested the stability of the complex (Fig. 4(III-D)). We found 3-5 H-bonds in the trajectory of 200 ns (Fig. 4 (III-E)). 2D interaction analysis of fortunellin-methyltransferase complex revealed five hydrogen bonds contributed by Thr6915, Val6916, Gln6957, Lys6958, and Val7092 (Fig. 4(III–F)). The total binding free energy suggests a stable complex formation with −23.1719 kcal/mol (Table 1). The energy was mainly contributed by the residues Ala6914, Thr6915, Val6916, Lys6933, and Phe6947 (Fig. 4 (III-G)).

3.10. MD simulation and MMGBSA analysis of fortunellin-nucleocapsid (N-NTD) complex

The atomistic dynamics movements and conformational variations of fortunellin-nucleocapsid (NTD) complex Cα backbone atoms revealed initial fluctuations in RMSD values up to 60 ns. A steady RMSD at 0.62 ± 0.04 nm was observed until the molecular simulation of 175ns (Fig. 5 (I-A)). This variation in RMSD indicates fortunellin conformational changes in the receptor pocket to acquire the optimal stable connections. A steady Rg value suggests a stable and compact structure (Fig. 5(I–B)). Furthermore, a minimal distance of 0.16–0.22 nm between the ligand and receptor confirmed the stability of the ligand-target complex. The key substrate-binding residues (with a 5 Å zone), with RMSF values ranging from 0.22 to 0.25 nm, were observed to be Arg89, Ala91, Thr92, Arg93, Tyr110, Arg150, Asn151, and Pro152 (Fig. 5(I-D)). We observed an average of four H-bonds during the simulation (Fig. 5(I-E)). We noticed that Arg89, Thr92, and Arg94 (two H-bonds) contributed to the H-bonds. Furthermore, we found that fortunellin was stabilized through non-polar and polar interactions, as shown in Fig. 5(I–F). These connections are strong enough to keep the complex structure intact, reducing the viral-RNA interaction and infectivity to the host. Energy calculations using MM-GBSA revealed total binding free energy of −16.9243 kcal/mol (Table 1). The residues Thr50, Ala51, Arg89, Ala91, Thr92, Arg93, Tyr110, Tyr112, Pro118, and Pro152 contributed to the stable binding energy (Fig. 5(I-G)).

3.11. MD simulation and MMGBSA analysis of fortunellin-nucleocapsid (N-CTD) complex

Similarly, the stability of the Nucleocapsid-CTD complex with fortunellin was examined. A RMSD value of 0.70 ±0 .12 nm (Fig. 5(II-A)) and an Rg value of 1.7 ± 0.1 nm suggested the stability, compactness, and integrity of the complex (Fig. 5(II–B)). We observed a conformational change after ~150 ns. The distance between fortunellin and N-CTD was found to be a minimum of 0.2 nm (Fig. 5(II–C)). The important residues had a low RMSF value of 0.25 nm on average throughout the simulation (Fig. 5 (II-D)). Three to four H-bonds between protein-ligand complex depict its stability (Fig. 5 (II-E)). We observed that Asn285, Pro309, Leu331, and Tyr333 showed H-bond. Fortunellin also showed non-polar hydrophobic, polar, and charged interaction (Fig. 5(II–F)). Notably, fortunellin has the highest binding affinity to the N-CTD compared to any target under consideration, as revealed by MM-GBSA energy calculations. The total binding free energy was found to be −54.6217 kcal/mol (Table 1). The residues that contributed to the stable binding energy were Arg277, Gly284, Asn285, Phe286, Leu291, Ile304, Ala308, Pro309, Ser310, Ala311, Ser312, Phe314, Phe315, Leu331, Tyr333, Leu353, and Ile357 (Fig. 5(II-G)).

3.12. Molecular and ADMET properties of fortunellin

The various molecular and physicochemical properties of fortunellin were calculated, and the observed results are listed in Supplementary Table S3. The molecular weight of fortunellin is 592.180 Da with14 H-bond acceptors and 7 H-bond donors. The number of rotatable bonds was found to be seven, thus providing enough flexibility to rotate about its axis and interact with the receptor residues. It constitutes five rings with ten atoms in the biggest ring. There exists no formal charge. The log of aqueous solubility (logS) of fortunellin is −3.891 mol/L, and the log of octanol/water partition coefficient (logP) is 0.568, indicating its nature to be more hydrophilic than hydrophobic. Also, the value of logP at physiological pH was found to be in an optimum range. After satisfactory results from the molecular features, fortunellin was further evaluated for its ADMET properties. We calculated the pharmacokinetic properties of fortunellin using ADMETlab 2.0, and pkCSM (Supplementary Table S4). We observed a preferable water solubility of −2.837log mol/L, with reliable gastric absorption that complied with the stated bioavailability score. We found that fortunellin was skin impermeable. It is also known as P-glycoprotein substrate, a cellular efflux pump that pumps drugs to extracellular fluid and does not inhibit any P-glycoprotein [46]. An optimum volume distribution (VDss) of 0.603 L/kg and 17.24% of the unbound fraction of the drug in the body were predicted. It showed a low probability of 0.293 for passing the blood-brain barrier (BBB) and thus would not cause any side effects to CNS. Moreover, the cytochrome P450 (CYP P450) enzymes family is not predicted to have any impact on encountering fortunellin in the body. The compound showed a probability of a short half-life time and thus would be consumed quickly without interfering with other cell functionalities. Fortunellin did not provoke skin sensitization and was not predicted to have AMES, hERG I & II, minnow, respiratory, and hepato-toxicity.

3.13. Identification of targets of fortunellin in COVID-19 infected host cells/organoids

We identified 129 host proteins that could be targeted by fortunellin (Supplementary Table S5) using SwissTargetPrediction (STP) [75] and the Similarity Ensemble Approach (SEA) [74]. We retrieved 500 up-regulated genes from SARS-CoV-2 infected human NHBE cells (GSE147507), lung cells (GSE147507), pancreatic organoids (GSE151803), colon organoids (GSE148696), liver organoids (GSE151803), and cornea organoids (GSE164073) using the Enrichr library “COVID-19 Related Gene Sets 2021.” In NHBE cells, fortunellin targets 11 genes, ten genes in lung cells, six genes in pancreatic organoids, eight genes in colon organoids, seven genes in liver organoids, and eight genes in cornea organoids (Fig. 6, Supplementary Table S6).

3.14. Functional enrichment analysis of gene targets of fortunellin in NHBE cells

In NHBE cells, we performed the functional enrichment analysis using the 11 gene targets of fortunellin, including FN1, PTGS2, TNF, IGFBP3, EPHA2, LGALS9, AKR1B1, XDH, MMP1, VEGFA, and IL6. The major biological processes (BPs) include positive regulation of acute

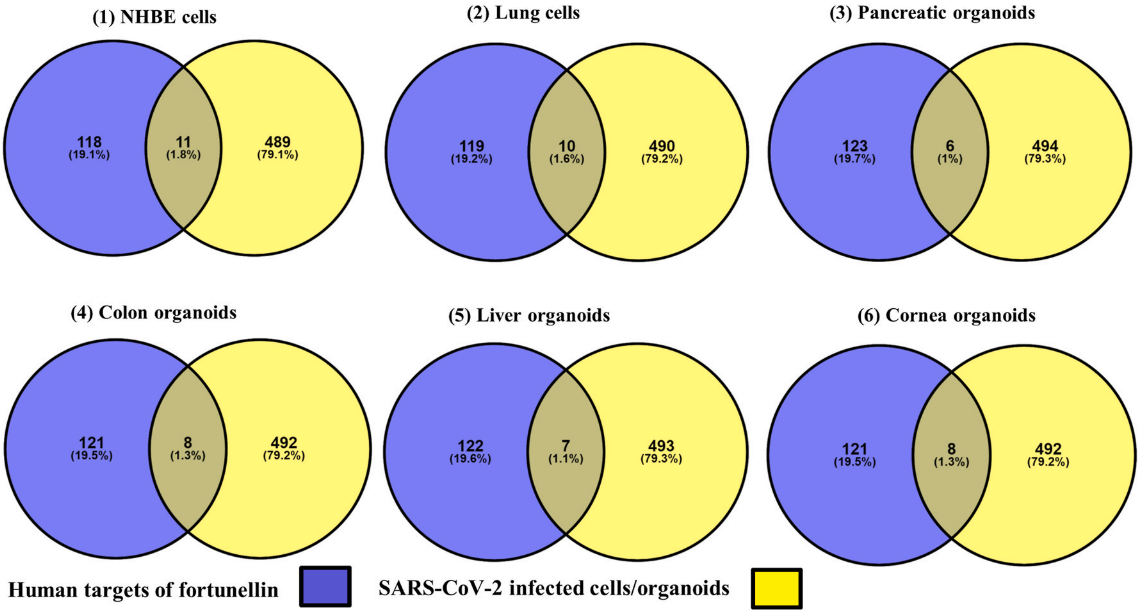

Fig. 6. Venn diagram showing targets of fortunellin in COVID-19 infected cells/organoids.

inflammatory responses, regulation of transforming growth factor-beta production, regulation of neuro-inflammatory responses, cytokine-mediated signaling pathway, positive regulation of leukocyte migration, regulation of the p38MAPK cascade, positive regulation of macromolecule metabolic processes, and regulation of chemokine production (Fig. 7-I). The major molecular functions enriched were cytokine activity, receptor-ligand activity, growth factor activity, growth factor receptor binding, and cytokine receptor binding (Fig. 7-I). The significant enriched cellular components include the endoplasmic reticulum lumen, platelet alpha granule lumen, and intracellular organelle lumen (Fig. 7-I).

3.15. Functional enrichment analysis of gene targets of fortunellin in lung cells

In lung cells, functional enrichment analysis was performed on the identified ten gene targets of fortunellin, i.e., TNF, ADRA2A, CYP19A1, LGALS9, CD38, CA12, HCAR2, MMP8, CASP1, and CA1. The major biological processes include negative regulation of lipid catabolic and metabolic processes, positive regulation of NIK/NF-kappaB signaling, positive regulation of interleukin-1 beta production, positive regulation of intracellular signal transduction, positive regulation of interleukin-6 production, and positive regulation of MAPK cascade (Fig. 7-III). The enriched molecular functions include cysteine-type endopeptidase activity involved in the apoptotic signaling pathway and; in the execution phase of apoptosis and tumor necrosis factor receptor binding (Fig. 7-III). Furthermore, the gene targets were associated with cellular components: collagen-containing extracellular matrix, tertiary granule lumen, and specific granule lumen (Fig. 7-III).

3.16. Functional enrichment analysis of gene targets of fortunellin in pancreatic organoids

In pancreatic organoids, the functional enrichment analysis was performed on TNF, ADRA2C, ECE1, LGALS1, ABCB1, and CBS gene targets of fortunellin. The biological processes were enriched in positive regulation of signaling, regulation of peptide hormone secretion, positive regulation of intracellular signal transduction, regulation of insulin secretion, regulation of protein secretion, positive regulation of (IkappaB kinase/NF-kappaB signaling, regulation of programmed cell death, regulation of fever generation, positive regulation of anion transmembrane transport, and cellular response (Fig. 7-VI). The enriched molecular functions and cellular components were primarily involved in protein homo-dimerization activity and the external side of the apical plasma membrane, clathrin-coated vesicle, and membrane raft (Fig. 7-VI).

3.17. Functional enrichment analysis of gene targets of fortunellin in colon organoids

In colon organoids, the gene targets including TNF, ADRA2C, ECE1, LGALS3, LGALS1, MMP7, MMP1, and ALDH1A2 were subjected to functional enrichment analysis. Analysis revealed the positive regulation of dendritic cell differentiation, positive regulation of leukocyte differentiation, positive regulation of cellular component biogenesis, regulation of dendritic cell differentiation, positive regulation of cellular component organization, regulation of protein-containing complex assembly, positive regulation of protein-containing complex assembly and regulation of mononuclear cell migration as the major biological processes. Metallo-endopeptidase and peptidase activity were the most common molecular functions (Fig. 7-IV). We also found that the gene targets were part of the collagen-rich extracellular matrix, the ficolin-1-rich granule membrane, and the clathrin-coated vesicles (Fig. 7-IV).

3.18. Functional enrichment analysis of gene targets of fortunellin in liver organoids

In SARS-CoV-2 infected liver organoids, the role of fortunellin was identified by performing the functional enrichment analysis using its upregulated gene targets, i.e., ACHE, NRAS, IGFBP3, FGF2, ERAP2, CASP7, and CASP1. The enriched biological processes and molecular functions included proteolysis, positive regulation of endothelial cell proliferation, regulation of endothelial cell proliferation, small GTPase mediated signal transduction, positive regulation of epithelial cell proliferation, Ras protein signal transduction, negative regulation of cell migration, glycerophospholipid biosynthetic process, positive regulation of cAMP, positive regulation of various cysteine-type endo-peptidase activity, insulin-like growth factor I&II binding, and protein phosphatase activator activity (Fig. 7-V). The cellular components were primarily involved in the endoplasmic reticulum lumen, basement membrane, tertiary granule membrane, and intracellular organelle lumen (Fig. 7-V).

3.19. Functional enrichment analysis of gene targets of fortunellin in cornea organoids

In cornea organoids, we used the eight gene targets of fortunellin: IL6, CA12, CYP1B1, ABCC1, CYP19A1, FN1, ANPEP, and ADAM17 to perform the functional enrichment analysis. We found that the enriched terms for the biological processes include myeloid leukocyte mediated immunity, regulation of leukocyte chemotaxis, positive regulation of vascular endothelial growth factor production, regulation of vascular endothelial growth factor production, positive regulation of leukocyte migration, estrogen metabolic process, positive regulation of receptor signaling pathway via STAT, positive regulation of receptor signaling pathway via JAK-STAT. Also, the molecular function analysis results revealed interleukin-6 receptor binding to be the essential function in which the gene targets of fortunellin are involved (Fig. 7-II). Furthermore, their involvement in cellular components of the endoplasmic reticulum lumen and membrane, intracellular organelle lumen, platelet alpha granule & its lumen, and organelle bounding membrane was discovered (Fig. 7-II).

3.20. PPI, module detection, and pathway enrichment analysis in NHBE cells, lung cells, pancreatic, colon, liver, and cornea organoids

In NHBE cells, we constructed the PPI network of 28 upregulated gene targets of fortunellin. A significant network module (20 nodes and 173 edges) was detected with an MCODE score of 18.211 (Fig. 8(A)). We found six key hub genes associated with the network module: VEGFA, TNF, IL6, FN1, PTGS2, and MMP1. The top five enriched pathways of the network modules' highlighted the fortunellin's role in the TNF signaling system, the IL-17 signaling pathway, the AGE-RAGE signaling pathway in diabetic complications, the NF-kappa B signaling pathway, and the relaxin signaling circuit (Table 2). In lung cells, we constructed a PPI network of 26 upregulated gene targets and found a significant module (18 nodes and 143 edges) with an MCODE score of 16.824 (Fig. 8(B)) that included key genes such as TNF, CASP1, and CD38, which are all targets of fortunellin. The pathways linked with the module included influenza A, cytokine-cytokine receptor interaction, viral-protein interaction with cytokine and cytokine receptor, toll-like receptor signaling pathways, and neutrophil extracellular trap formation (Table 2). In pancreatic organoids, 11 gene targets were used to construct a PPI, and a module (5 nodes and 10 edges) with an MCODE score of 5.00 was found (Fig. 8(C)). We found that fortunellin targets the module's TNF gene. The adipocytokine signalling pathway, insulin resistance, lipid and atherosclerosis, inflammatory bowel disease, and the AGE-RAGE signalling pathway in diabetic complications were unearthed through the module's pathway enrichment analysis (Table 2). In colon organoids, 26 gene targets were used to build a PPI, and a module (16 nodes and 104 edges) with an MCODE score of 13.867 was found (Fig. 8(D)). TNF, MMP1, and MMP7 were identified as crucial genes that served as a hub for the module and were fortunellin targets. Rheumatoid arthritis, the IL-17 signalling pathway, the TNF signalling pathway, lipid and atherosclerosis, and the NF-kappa B signalling pathway are among the results of the pathway enrichment analysis (Table 2). In liver organoids, a PPI was constructed using 11 gene targets, a module with 5 nodes and 10 edges and an MCODE score of 5.0 was found (Fig. 8(E)). Furthermore, we identified two key genes, CASP1 and FGF2, which served as network hubs. The top five pathways linked with the network module include influenza A, lipid and atherosclerosis, AGE-RAGE signaling pathway in diabetic complications, TNF signaling route, and the NOD-like receptor signaling pathway (Table 2). Similarly, in cornea organoids, a PPI with 12 gene targets was created, and a module with 6 nodes and 14 edges was found with an MCODE score of 5.60. (Fig. 8(F)). We identified three key genes, IL6, ANPEP, and FN1, which acted as the hub of the module and were fortunellin targets. Fortunellin has been associated with a variety of biological pathways, including hematopoietic cell lineage, AGE-RAGE signalling pathway in diabetic complications, PI3K-Akt signalling system, ECM-receptor interaction, and TNF signalling pathway (Table 2).

4. Discussion

Because of the high replication rate, a SARS-CoV-2 infection generates more than one million virions in one day [80], and most known antivirals are ineffective against it due to SARS- CoV-2's inherent genetic mutability [84–86]. COVID-19 patients showed respiratory symptoms, multi-organ dysfunction, and inflammation [2–4]. Therefore, in comparison to single target approaches, concurrent inhibition of multiple SARS-CoV-2 targets [87,88] combined with inflammation and immunomodulation associated with tissue-specific host targets may be more effective and have a significantly higher therapeutic potential in saving the life of a COVID-19 patient. In this study, we discovered that fortunellin, a naturally occurring flavonoid O-glycoside molecule, exhibits multi-targeting potential against key SARS-CoV-2 target proteins. We have also found the possible human targets of fortunellin in SARS-CoV-2 infected tissues. These include human NHBE cells, lung cells, pancreatic organoids, colon organoids, liver organoids, and cornea organoids.

Fortunellin, one of the constituents of Gojihwadi Kwath, an Indian traditional-Ayurvedic formulation, is known to have antioxidant and ant-inflammatory biological properties in animals [89,90] and can also be extracted from *Citrus japonica* var. *margarita* fruits [41]. Traditionally, the Gojihwadi Kwath is well known to have antiviral properties and has been used in COVID-19 treatment and management [42–45]. However, the mechanism of its antiviral activity remains unknown. It was recently found that fortunellin inhibits Mpro dimerization [46]. Fortunellin has also been shown to exhibit inhibitory activity against HIV-1 protease [47], as well as antibacterial properties [48]. Furthermore, fortunellin's pharmacodynamic–pharmacokinetic properties show that it is water-soluble with low absorption in the GI tract; fortunellin is non-toxic because it does not interact with the CYPs involved in drug metabolism; and fortunellin is a substrate of the P-glycoprotein 1 (Pgp or MDR1) multidrug transporter, implying rapid elimination from the body (Supplementary Table S3 and S4) [46]. As an outcome, the application of fortunellin's multi-target potentials for the therapy of COVID-19 could be promising. This prompted us to examine the effect of fortunellin on the key targets of SARS CoV-2, including Mpro, PLpro, RdRp, NendoU, replicase (monomer and dimer forms), Helicase, 2′O-methyltransferase, N-NTD, and N-CTD, all of which are considered necessary for viral replication, growth, invasion, and infectivity. The negative binding energies of the docked complex of fortunellin-SARS-CoV-2 targets (Fig. 1, Supplementary Figure S1, and Table S1 (B)) allowed us to propose that fortunellin may act as a potential multi-target drug against COVID-19. Additionally, to validate the reliability and interaction stability of the docked complexes, we performed 200 ns long MD simulations of each of the twelve fortunellin-target complexes that resulted in a total of 2.2 μs long molecular trajectories. We found that all the complexes were stable throughout the run, as indicated by their steady RMSD values and low and stable Rg values. Also, the minimum distance between the fortunellin-target complexes was stable, indicating that the ligand was in close proximity to the receptor throughout 200 ns. A stable residue fluctuation (RMSF value) of the residues of ligand binding site in all the fortunellin-target complexes suggests the favorable accommodation of fortunellin. Next, through MD simulation, we intend to evaluate the binding affinity of the fortunellin–target complexes and identified the key residues contributing to their affinity. We validated and computed the binding free energy of the ligand-target complexes using MM-GBSA. The MM/GBSA approach is widely used to examine receptor-ligand interaction. For the MM-GBSA calculations, we extracted 1000 snapshots at every five ps intervals from the last 50 ns MD trajectory. The negative binding free energy, which ranges from −54.62 to −16.81 kcal/mol, indicates that fortunellin-target complexes are stable, including N-CTD (−54.62 kcal/mol) at the top of the list, followed by

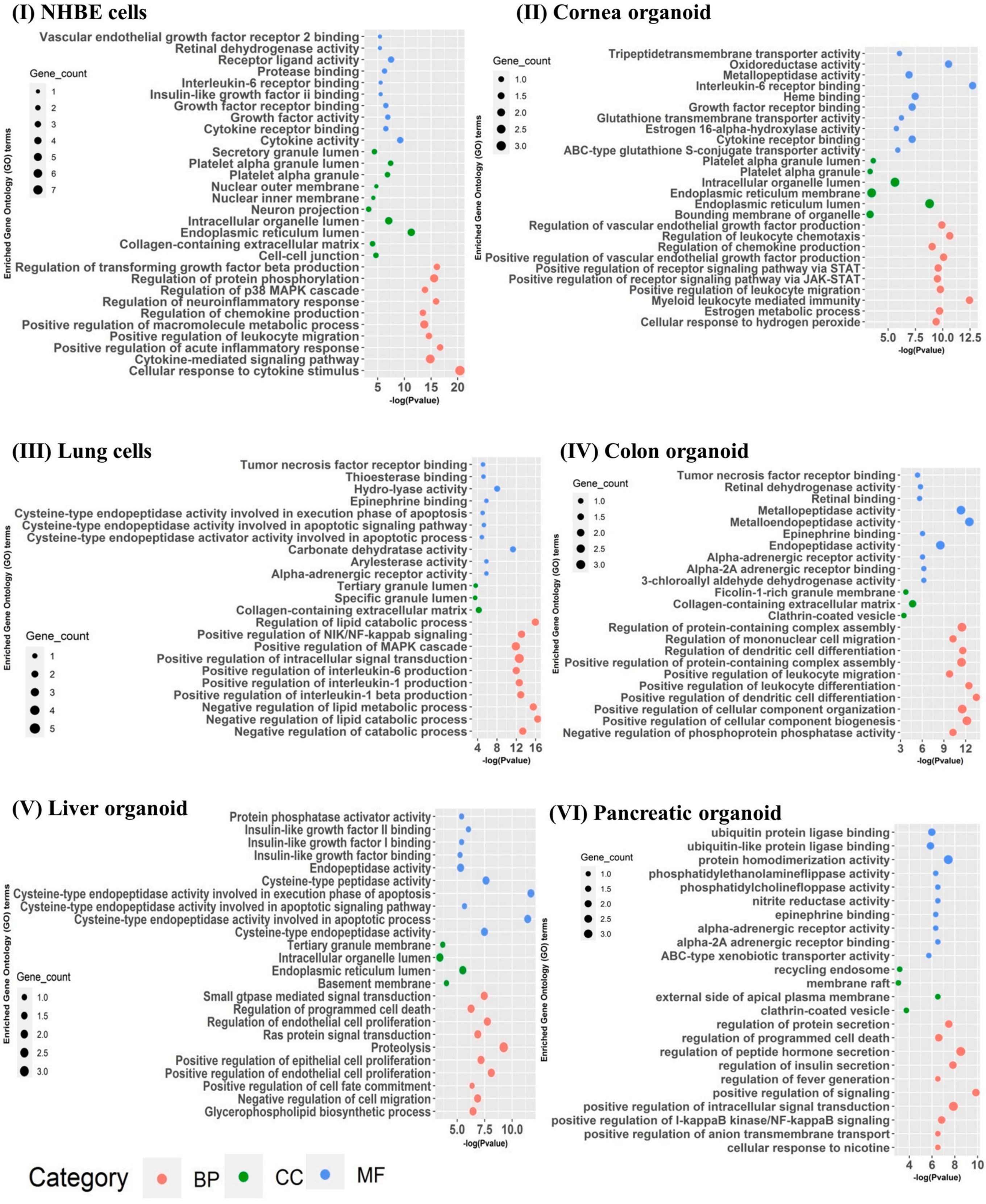

Fig. 7. Functional enrichment analysis of upregulated genes targets fortunellin in COVID-19 infected cells/organoids. The details of the genes of the GO terms are provided in Supplementary Table S7 (A–F).

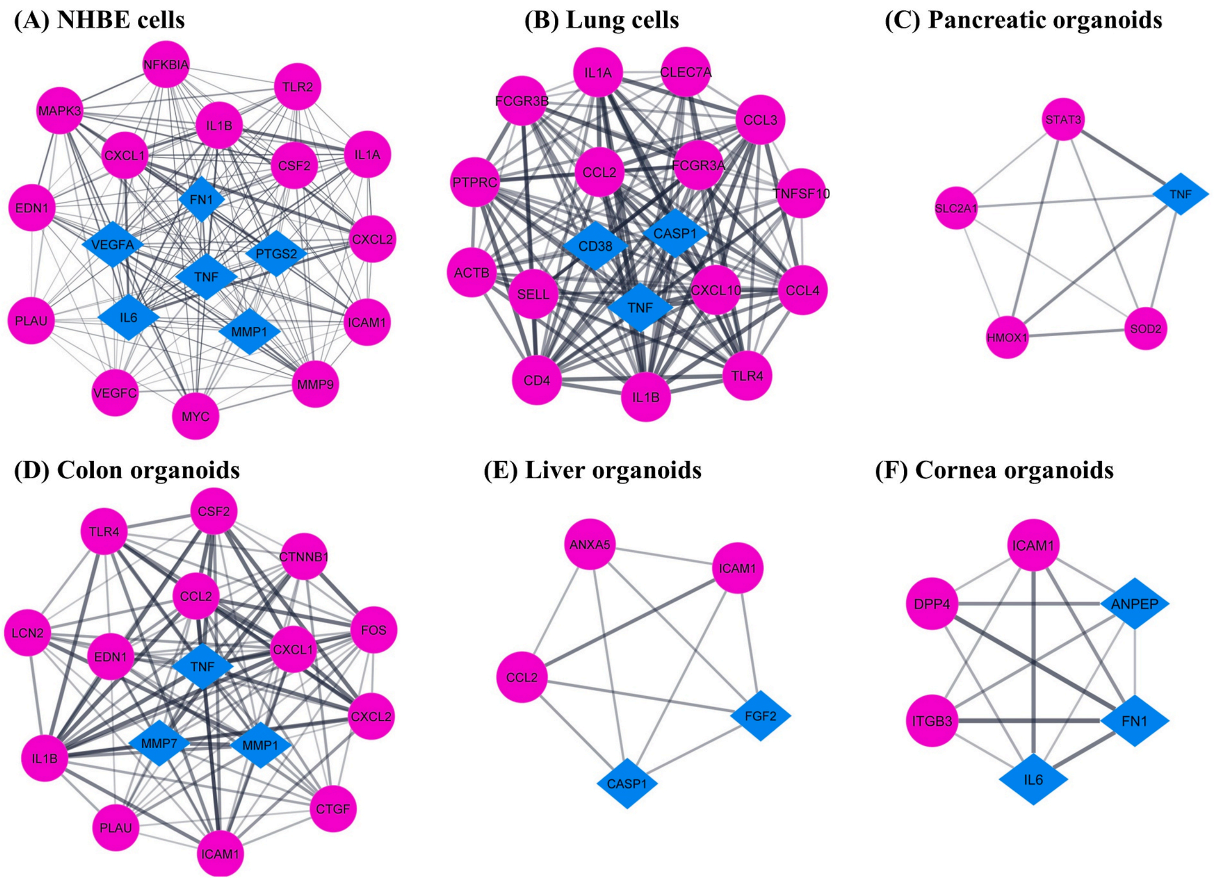

Fig. 8. Modules and hub gene targets of fortunellin. Hub genes targeted by fortunellin in COVID-19 infected cells/organoids are shown in blue diamonds. The upregulated neighbors of the fortunellin targets are depicted in a pink circle.

Replicase-monomer-non-structural protein (NSP)-8 binding site (−34.48 kcal/mol), Replicase-dimer (−31.29 kcal/mol), Helicase (−30.02 kcal/mol), Papain-like-protease (−28.12 kcal/mol), 2′-O-methyltransferase (−23.17 kcal/mol), Main-protease (−21.63 kcal/mol), Replicase-monomer at dimer interface (−22.04) kcal/mol, RNA-dependent-RNA-polymerase (−19.98 kcal/mol), Nucleocapsid-NTD (−16.92 kcal/mol), and Endoribonuclease (−16.81 kcal/mol) (Table 1). We decomposed the binding energy $\Delta G_{\text{MM-GBSA}}$ by residue to get a more precise thermodynamic description of the residue contributions [91]. The decomposition method helped identify residues involved in receptor-ligand interactions. Masking these residues via fortunellin may prevent them from participating in their molecular functions.

A comparison of the N3-Mpro (NSP5) co-crystal structure (PDB ID: 6LU7) with the fortunellin-Mpro docked complex revealed that fortunellin inherited the key interactions that are featured by N3, including hydrogen bonds with Cys145 and Glu166. These interactions likely stabilize the fortunellin in the binding pocket and increase the binding affinity. The residue decomposition analyses based on 200 ns MD simulation analysis revealed the key residues, including Thr25, His41, Cys145, Met149, Met165, and Gln189, that stabilize the fortunellin-Mpro complex. Also, we found that fortunellin fully occupies the active site, which likely explains the good MMGBSA score. Moreover, the residue contribution analysis reveals that catalytically and functionally important residues His41, Gly143, Cys145, and Gln189 contribute to binding with the ligand. This is consistent with the reports [92–94] that noted these residues are key players in ligand interactions with Mpro. Thus, fortunellin targeting Mpro may be considered a potential blocker of viral replication during the COVID-19 infection.

To evaluate the binding affinity of fortunellin with PLpro (NSP3), we used the crystal structures of SARS-CoV-2 PLpro in a complex with a peptide inhibitor VIR251 (PDB ID: 6WX4) [95]. Interestingly, the binding mode of fortunellin appears to be similar to VIR-251. Our docking studies showed that fortunellin binds to the active site and interacts with His272, therefore likely hindering the catalytic triad of Cys111, His272, and Asp286 and suggesting its inhibitory role (Fig. 2 (II–F)). Like VIR-251, fortunellin also showed interactions with the residues Tyr268, Gly271, and Tyr264 [95]. Furthermore, we discovered that the hydrophobic interactions Leu162, Pro248, Ala249, Tyr264, Tyr268, Cys270, and Pro299 help to stabilize the binding interactions. Furthermore, MMGBSA-based residue decomposition analyses revealed that the Pro248, Tyr264, Tyr268, and Cys270 residues majorly contributed to the reliable total binding free energy value of −28.1218 kcal/mol (Table 1), favoring the PLpro-fortunellin complex formation.

The SARS-CoV-2 RdRP (NSP12) was found to be targeted by Remdesivir, Molnupiravir, Favipiravir, and Galidesivir antivirals [96–99]. We compared the residues interacting with the Remdesivir [PDB ID: 7BV2] and found that fortunellin binds to the active site similarly. Ala547, Ile548, Ser549, Ala550, Lys551, Asn552, Arg555, and Lys798 contributed to the favorable energy in the fortunellin-RdRp complex stabilization (Fig. 2 (III-G)). Thus, targeting the RdRp active sites with fortunellin could be a potential therapeutic option. RdRp catalytic residues ^{759}SDD^{761} and the divalent-cation-binding residue D618 were stabilized. Although Remdesivir showed clinical benefits in patients with severe COVID-19, it was ineffective in improving survival, and hence a molecule like fortunellin could be a promising oral drug.

The inhibitor tipiracil or modified RNA with 2′-fluorine on the uridine ribose targets NendoU (Nsp15) (PDB ID: 6WXC) [100]. We found that fortunellin effectively binds to the active site of NendoU like tipiracil. The binding free energy calculations using the MMGBSA analysis revealed a reliable binding free energy of −16.8122 kcal/mol (Table 1).

Table 2
Pathway enrichment analysis of genes of network modules.

Pathways	Gene count	Genes	Adjusted p-value
NHBE cells			
TNF signaling pathway	13	EDN1, CSF2, VEGFC, CXCL1, PTGS2, MMP9, CXCL2, TNF, ICAM1, NFKBIA, IL6, IL1B, MAPK3	1.94E-25
Rheumatoid arthritis	11	IL1A, IL6, CSF2, MMP1, IL1B, CXCL1, CXCL2, TNF, VEGFA, ICAM1, TLR2	1.93E-21
IL-17 signaling pathway	11	NFKBIA, IL6, CSF2, MMP1, IL1B, CXCL1, PTGS2, MMP9, CXCL2, TNF, MAPK3	2.19E-21
AGE-RAGE signaling pathway in diabetic complications	10	IL1A, EDN1, IL6, IL1B, FN1, VEGFC, TNF, VEGFA, ICAM1, MAPK3	1.09E-18
Lipid and atherosclerosis	11	NFKBIA, IL6, MMP1, IL1B, CXCL1, MMP9, CXCL2, TNF, ICAM1, MAPK3, TLR2	2.64E-17
Lung Cells			
Influenza A	8	IL1A, CXCL10, IL1B, CASP1, CCL2, TNF, TLR4, ACTB	3.18E-12
Rheumatoid arthritis	6	IL1A, IL1B, CCL3, CCL2, TNF, TLR4	4.83E-10
Cytokine-cytokine receptor interaction	7	IL1A, CXCL10, CD4, IL1B, CCL3, CCL2, TNF	5.68E-09
Toll-like receptor signaling pathway	5	CXCL10, IL1B, CCL3, TNF, TLR4	4.34E-08
NOD-like receptor signaling pathway	5	IL1B, CASP1, CCL2, TNF, TLR4	4.22E-07
Pancreatic organoids			
Adipocytokine signaling pathway	3	STAT3, SLC2A1, TNF	3.79E-05
Insulin resistance	3	STAT3, SLC2A1, TNF	5.05E-05
Lipid and atherosclerosis	3	STAT3, SOD2, TNF	2.92E-04
Inflammatory bowel disease	2	STAT3, TNF	0.002005
AGE-RAGE signaling pathway in diabetic complications	2	STAT3, TNF	0.003396
Colon organoids			
Rheumatoid arthritis	10	CSF2, MMP1, IL1B, CCL2, CXCL1, FOS, CXCL2, TNF, TLR4, ICAM1	2.24E-20
IL-17 signaling pathway	9	CSF2, MMP1, IL1B, LCN2, CCL2, CXCL1, FOS, CXCL2, TNF	8.40E-18
TNF signaling pathway	9	EDN1, CSF2, IL1B, CCL2, CXCL1, FOS, CXCL2, TNF, ICAM1	4.32E-17
Lipid and atherosclerosis	9	MMP1, IL1B, CCL2, CXCL1, FOS, CXCL2, TNF, TLR4, ICAM1	1.74E-14
NF-kappa B signaling pathway	7	PLAU, IL1B, CXCL1, CXCL2, TNF, TLR4, ICAM1	9.22E-13
Liver organoids			
Influenza A	3	CASP1, CCL2, ICAM1	6.17E-06
Lipid and atherosclerosis	3	CASP1, CCL2, ICAM1	1.21E-05
AGE-RAGE signaling pathway in diabetic complications	2	CCL2, ICAM1	2.45E-04
TNF signaling pathway	2	CCL2, ICAM1	3.07E-04
NOD-like receptor signaling pathway	2	CASP1, CCL2	8.00E-04
Cornea organoids			
Hematopoietic cell lineage	3	IL6, ANPEP, ITGB3	2.33E-06
AGE-RAGE signaling pathway in diabetic complications	3	IL6, FN1, ICAM1	2.40E-06
PI3K-Akt signaling pathway	3	IL6, ITGB3, FN1	1.06E-04
ECM-receptor interaction	2	ITGB3, FN1	2.84E-04
TNF signaling pathway	2	IL6, ICAM1	4.59E-04

Lys290, Ser316, Met331, Trp333, Cys334, Glu340, Thr341, and Tyr343 with negative binding energy suggest the favorable fortunellin-endoribonuclease complex formation. The H-bond contributed by Cys334 and Glu340 conferred stability to the complex (Fig. 3 (I–F)). We observed that fortunellin interacts with His235 and Lys290. These residues constitute the catalytic triad and His250 [100,101]. Also, conserved amino acid residues including His235, Lys290, Thr341, Trp333, Tyr343, His250, Ser294, Gly248, Lys345, Val295, and Gln245 were found to interact with fortunellin, thereby masking the functional site. These residues are involved in substrate specificity, nuclease activity, and oligomerization of NendoU [100,101]. Therefore, fortunellin like tipiracil may potentially interfere with the stability and activity of NendoU and could be an effective inhibitor.

We have utilized the well-characterized and druggable pocket located on the dimer's surface and near the monomer-monomer interface of replicase (NSP9) (PDB ID: 6W4B) [83,102]. A computational study has shown that the replicase monomer pocket harbors small molecules such as Simeprevir, Darunavir, and Rimantadine [102]. Simeprevir, a potent suppressor of SARS-CoV-2 replication, interacts with the residues Leu46, Cys74, Arg75, Phe76, Lys87, Leu89, Phe91, Leu104, Leu107, Ala108, Val111, and Leu113 [102]. We have found that fortunellin occupies the same location and interacts with the residues Gln12, Leu30, Tyr32, Leu46, Phe76, Thr78, Lys87, Leu107, Thr110, Val111, and Leu113 of chain A. Furthermore, we have chosen a cavity of the protein mediating homodimer formation [103]. We found that fortunellin interacts with the residues Met1, Asn2, Asn3, Pro7, Val8, Leu98, Arg100, Gly101, Met102, Val103, Leu104, Gly105, and Ala108. Our result suggests that fortunellin could inhibit monomer-monomer interactions to prevent replicase-dimer formation.

Next, fortunellin binds to a region of the replicase, mediating homodimer formation [103]. This site was also targeted by an ent-kaurane natural product, oridonin [104], and its clinical analog HAO472 [105] inhibits SARS-CoV-2 replication. We compared the residues interacting with the Oridonin and prodrug HAO472 and found that fortunellin binds to the dimer binding site. Notably, we observed that fortunellin interacts with the Cys74, a key residue within the replicase protein that interacts with oridonin and HAO472. MMGBSA analysis of fortunellin-replicase (dimer) complex yielded an overall binding free energy of −31.2907 kcal/mol. As shown in (Fig. 4 (I-G)), residues of both the chains contributed to the negative free energy including Met1, Leu5, Ser6, Pro7, and Val8 residues of Chain A and Cys74, Arg75, Phe76, Val77, Leu107, Val111 and Leu113 residues of Chain B, respectively. Thus, fortunellin binding to the cavity at the dimeric contact point of replicase may prevent it from binding with RNA and NSP-8 essential for viral propagation. Conclusively, our result suggests that fortunellin could either disrupt pre-formed replicase-dimers or may prevent replicase-dimer formation by inhibiting monomer-monomer interactions.

The binding site of the SARS-COV-2 helicase (NSP13) is located between the 1A and 2A domains, comprising important amino acids necessary for ATP binding; Asp374, Glu375, Ser377, Asp401, Gln404, Arg443, Lys288, Ser289, Arg567, and Gly538 (PDB ID: 5RLG). Experimental and in-silico studies have also been reported targeting the helicase with different molecules [106–111]. We docked the fortunellin into the active site of the SARS-CoV-2 helicase and found that it achieved a better docking score of −9.8 kcal/mol than the re-docked co-crystallized ligand. Interestingly, fortunellin could stably occupy the ATP binding domain, forming four hydrogen bonds contributed by Ser289 (two H-bonds), Lys320, and Glu375. We observed that the catalytically important residues His290, Arg442, and Arg443, contributed to the binding free energy. Also, Pro283, Gly285, Thr286, Gly287, Ser289, Ala312, Ala313, Ala316, Leu317, Asp374, Glu375, Ile399, Gln537, Gly538, Ser539, and Glu540 were found to be contributing toward the negative binding free energy (Fig. 4 (II-G)). Fortunellin binding to the ATP binding site may disrupt the ATP binding and inhibit the SARS-CoV-2 helicase and could be regarded as a potential drug for treating COVID-19.

We report that fortunellin occupies the SAM and its analogs (such as sinefungin [SFG]) binding pocket of 2′-O-methyltransferase (NSP16; PDB ID 6W4H) and, therefore, may inhibit its activity. Since several residues that participate in catalysis and SAM binding are conserved and homologous to other coronaviruses [112,113], fortunellin as a methyltransferase inhibitor could be a promising broad-spectrum antiviral candidate. Experimental and in-silico studies have shown the inhibitory potential of the different molecules against the SARS-CoV-2 methyltransferase [14,114–116]. We report that in fortunellin-2′-O-methyltransferase complex (Fig. 4 (III–F), fortunellin has interactions similar to SAM. Fortunellin-methyltransferase complex revealed five hydrogen bonds contributed by Thr6915, Val6916, Gln6957, Lys6958, and Val7092 (Fig. 4 (III–F)). We observed that fortunellin accommodates an adjacent cavity of the RNA methylation site. However, its bulkier size and stable binding may hinder the incoming RNA and the methylation process (Fig. 4 (III–F)). The total binding free energy of −23.1719 kcal/mol suggests a stable complex formation. The energy was mainly contributed by the residues Ala6914, Thr6915, Val6916, Lys6933, and Phe6947 (Fig. 4 (III-G)).

Based on the available experimental and computational studies, we have chosen the druggable pocket located on the surface of the nucleocapsid N-terminal RNA binding domain (PDB ID: 6M3M). The pocket has been shown to bind with the small molecule via Ala91, Thr92, Arg93, Arg94, Ile95, Asp104, Leu105, Ser106, Arg108, Tyr110, Tyr112, and Arg150 [40,117–120]. The drug Naproxen binds and interacts with the key residues Thr50, Ala51, Tyr112, and Arg150 [119]. Also, in vitro assays indicated that the phenanthridine derivatives could bind to the N-NTD cavity to inhibit the SARS-CoV-2 replication [121]. We have found that fortunellin occupies a similar location and interacts with the residues Thr50, Ala51, Arg89, Ala91, Thr92, Arg93, Tyr110, Tyr112, Pro118, Arg150, Asn151, and Pro152 (Fig. 5 (I-D, and I-G)). Notably, H-bonds contributed by Arg89, Thr92, and Arg94 (two H-bonds) may provide stability to the fortunellin-N-NTD complex, impeding the viral-RNA interaction and infectivity to the host.

Next, we found that fortunellin binds to the SARS-CoV-2 nucleocapsid protein (PDB entry: 6WJI) at residues 257–364 of the C-terminal dimerization domain [122]. Computational and in-vitro studies have reported that p-cymene, a natural monoterpene, impairs SARS-CoV-2 replication by binding to the CTD part of SARS-CoV-2 nucleocapsid protein [123,124]. A polyphenol from green tea, Gallocatechin gallate (GCG), is also reported to bind to nucleocapsid protein and inhibits SARS-CoV-2 replication [125]. Notably, our study revealed that fortunellin showed the highest binding affinity of −54.6217 kcal/mol to the N-CTD compared to any other target under consideration. We observed that fortunellin interacts with the residues that contributed to the stable binding energy were Arg277, Gly284, Asn285, Phe286, Leu291, Ile304, Ala308, Pro309, Ser310, Ala311, Ser312, Phe314, Phe315, Leu331, Tyr333, Leu353, and Ile357 (Fig. 5 (II-G)). We noted that Asn285, Pro309, Leu331, and Tyr333 showed H-bond (Fig. 5 (II–F)). Our findings thus present fortunellin as a potential compound against the nucleocapsid of the SARS-CoV-2. The N-NTD and N-CTD proteins are highly conserved in the coronavirus family [126]. Therefore, targeting nucleocapsid proteins using fortunellin may provide a novel avenue against SARS-CoV-2 and future variants of coronavirus.

Next, we employed the network pharmacology strategy to reveal the effect of fortunellin on the host system as an inhibitor of the upregulated genes responsible for excess inflammation and failure of immune responses. The role of fortunellin was explored in normal human bronchial epithelial cells, lung cells, and pancreatic, colon, liver, and cornea organoids. We have noted that in the SARS-CoV-2 infected six tissues, 36 genes were upregulated and targeted by fortunellin, including ABCB1, ABCC1, ACHE, ADAM17, ADRA2A, ADRA2C, AKR1B1, ALDH1A2, ANPEP, CA1, CA12, CASP1, CASP7, CBS, CD38, CYP19A1, CYP1B1, ECE1, EPHA2, ERAP2, FGF2, FN1, HCAR2, IGFBP3, IL6, LGALS1, LGALS3, LGALS9, MMP1, MMP7, MMP8, NRAS, PTGS2, TNF, VEGFA, and XDH. Among them, we have found that 11 upregulated genes, i.e., TNF, IL6, ANPEP, CASP1, CD38, FGF2, FN1, MMP1, MMP7, PTGS2, and VEGFA, were associated with functionally important modules (Fig. 7). The involvement of these genes in various biologically important pathways, including anti-inflammatory, immunomodulatory, and apoptotic pathways, suggests that fortunellin plays a protective role in the host system. The TNF and IL6 genes encode proteins involved in regulating inflammatory processes. It has been observed that serum TNF-α [127] and IL6 [128] levels are elevated in patients with COVID-19 and are higher with more severe diseases. We noticed that elevated expression of TNF is associated with four cells/organoids, i.e., normal human bronchial epithelial cells, lung cells, and pancreatic and colon organoids. Cell surface protein ANPEP (analylaminopeptidase membrane), the target of fortunellin, has been reported to promote SARS-CoV-2 entry into target cells [129]. Inflammasome activation was observed in COVID-19 patients' peripheral immune cells and tissues, and the level of inflammasome-derived products, including active caspase-1, was associated with disease severity and poor outcomes [130]. Horenstein et al. showed that CD38 plays a central role in altered immune metabolism resulting from COVID-19 infection and may be a promising therapeutic target of fortunellin [131]. The hyper-expression of FGF2 could be implicated in the pathogenesis of coronavirus infections by inducing apoptosis [132]. Therefore, inhibiting its signaling might represent a promising target for fortunellin [133]. Alveolar M2 macrophages produce fibro-proliferative markers, such as MMP7, which promote fibrogenesis, leading to lung stiffening; thus, their elevated expression is more vulnerable to COVID-19 infections [134,135]. Plasma MMP-1 enzymatic activity and plasma levels of MMP-1 and VEGF-A were significantly elevated in critical COVID-19 patients [136]. Excessive expression of MMP-1 plays a central role in tissue destruction in various vascular diseases. Upregulated VEGF-A, an endothelial cell (EC) activation marker, increases vascular permeability [137]. Excessive MMP-1 and hyperactivation of ECs occur in COVID-19 patients and are associated with the severity of COVID-19. Prostaglandin-endoperoxide synthase 2 (*PTGS2*) or Cyclo-oxygenase2 (Cox-2) is an inducible pro-inflammatory enzyme required for efficient entry and RNA replication. An effective COX-2 inhibitor during early viral infection may enhance and/or prolong endogenous interferon responses, thereby increasing anti-viral immunity [138,139]. Thus, the upregulated TNF, IL6, ANPEP, CASP1, CD38, FGF2, FN1, MMP1, MMP7, PTGS2, and VEGFA could be promising therapeutic targets of fortunellin. In the future, fortunellin can undergo further investigations in vitro and in vivo to unravel its antiviral action against COVID-19 treatment. The use of phytochemical fortunellin could be promising to minimize the side effects which are otherwise caused by the use of synthetic drug molecules.

5. Conclusion

Due to the inherent genetic mutability of SARS-CoV-2, most existing antivirals are ineffective against it. This necessitates the investigation of concurrent inhibition of several SARS-CoV-2 targets combined with anti-inflammatory and immunomodulatory effects. We report that fortunellin has a dual role; antiviral activities against SARS-CoV-2 and anti-inflammatory-immunomodulatory capabilities against the host. Molecular docking studies gave us the preliminary idea of the inhibitory action of fortunellin on the key targets of SARS-CoV-2. Molecular dynamics simulations validated the stability of the docked complexes. The results from the energy calculations through the MM-GBSA technique indicated the extent of interaction between the catalytically important residues of each protein with fortunellin. Thus, masking these residues makes them unavailable to participate in their functions. We found that fortunellin, reliably binds to key targets that are necessary for viral replication, growth, invasion, and infectivity, including nucleocapsid-CTD (−54.62 kcal/mol), Replicase-monomer-non-structural protein (NSP)-8 binding site (−34.48 kcal/mol), Replicase-dimer (−31.29 kcal/mol), Helicase (−30.02 kcal/mol), Papain-like-protease (−28.12 kcal/mol), 2′-O-methyltransferase (−23.17 kcal/mol), Main-protease (−21.63 kcal/mol), Replicase-monomer at dimer interface (−22.04) kcal/mol, RNA-dependent-RNA-polymerase (−19.98 kcal/mol), Nucleocapsid-NTD (−16.92 kcal/mol), and Endoribonuclease (−16.81 kcal/mol). Furthermore, we have identified and evaluated the potential human targets of fortunellin and its effect on the SARS-CoV-2 infected cells, including normal-human-bronchial-epithelium (NHBE) cells, lung cells, and organoids such as pancreatic, colon, liver, and cornea using a network pharmacology approach. The network pharmacology analysis revealed elevated TNF, IL6, ANPEP, CASP1, CD38, FGF2, FN1, MMP1, MMP7, PTGS2, and VEGFA to be promising therapeutic targets of fortunellin in the host system. Fortunellin is a promising candidate for preventing and treating COVID-19 by supporting protective immunity, inhibiting pro-inflammatory cytokines, inhibiting viral infection and replication, inducing apoptosis, and protecting against tissue damage. Given fortunellin's oral bioavailability and safety, this study could develop fortunellin as an orally active therapeutic against SARS-CoV-2 and new variants of coronavirus. However, its clinical usage on COVID-19 patients is a subject of further in-vivo and in-vitro investigations and clinical trials.

Author contributions statement

S.A. performed the computational experiments and prepared the illustrations; E.P. performed energy calculations and analysis. S.A. E.P., and R.M. analyzed the data and wrote the manuscript. V.M. and A.P. helped in the experiments. S.K.M.; P.S.B, S.D, A.K.C, V.M.S., R.N.C., and N.A. contributed to various aspects of the work. All authors have read and agreed to the published version of the manuscript. R.M. conceived, designed, and supervised the whole study of the research.

Declaration of competing interest

The authors declare that there are no conflicts of interest with the contents of this article.

Acknowledgments

A research fellowship supports Shivangi Agarwal and Vibha Mishra from Banaras Hindu University. Afifa Parveen is supported by CSIR-SRF, Govt. of India. R.M. gratefully acknowledges the research support from the IoE, Banaras Hindu University, and DST-CURIE-2022-80 (G), Govt. of India. We acknowledge the National medicos organization, Gausewa Sewa Bharti, Rashtriya Kamdhenu Ayog, Lok Ayurved, Arogya Bharti, and Vishwa Ayurved Parisad. We also thank Prof. A. K. Tripathi, Director, Institute of Science, BHU, and Prof. Inu Mehta, MMV, BHU, for their support.

Appendix A. Supplementary data

Supplementary data related to this article can be found at https://doi.org/10.1016/j.compbiomed.2022.106049.

References

[1] W.H. Organization, WHO Coronavirus Disease (COVID-19) Dashboard, covid19.who.int.
[2] A. Gupta, M.V. Madhavan, K. Sehgal, N. Nair, S. Mahajan, T.S. Sehrawat, B. Bikdeli, N. Ahluwalia, J.C. Ausiello, E.Y. Wan, Extrapulmonary manifestations of COVID-19, Nat. Med. 26 (2020) 1017–1032.
[3] X. Yao, T. Li, Z. He, Y. Ping, H. Liu, S. Yu, H. Mou, L. Wang, H. Zhang, W. Fu, A pathological report of three COVID-19 cases by minimally invasive autopsies, Zhonghua bing li xue za zhi= Chinese journal of pathology 49 (2020). E009-E009.
[4] E. Pathak, N. Atri, R. Mishra, Single-cell transcriptome analysis reveals the role of pancreatic secretome in COVID-19 associated multi-organ dysfunctions, Interdiscipl. Sci. Comput. Life Sci. (2022) 1–16.
[5] D.-G. Ahn, H.-J. Shin, M.-H. Kim, S. Lee, H.-S. Kim, J. Myoung, B.-T. Kim, S.-J. Kim, Current status of epidemiology, diagnosis, therapeutics, and vaccines for novel coronavirus disease 2019 (COVID-19), J. Microbiol. Biotechnol. 30 (2020) 313–324.
[6] R.K. Gupta, Will SARS-CoV-2 variants of concern affect the promise of vaccines? Nat. Rev. Immunol. 21 (2021) 340–341.
[7] S. Nasreen, H. Chung, S. He, K.A. Brown, J.B. Gubbay, S.A. Buchan, D.B. Fell, P. C. Austin, K.L. Schwartz, M.E. Sundaram, Effectiveness of COVID-19 vaccines against symptomatic SARS-CoV-2 infection and severe outcomes with variants of concern in Ontario, Nat. Microbiol. 7 (2022) 379–385.
[8] D. Tian, Y. Sun, H. Xu, Q. Ye, The emergence and epidemic characteristics of the highly mutated SARS-CoV-2 Omicron variant, J. Med. Virol. 94 (6) (2022) 2376–2383.
[9] S.A. Madhi, G. Kwatra, J.E. Myers, W. Jassat, N. Dhar, C.K. Mukendi, A.J. Nana, L. Blumberg, R. Welch, N. Ngorima-Mabhena, Population immunity and Covid-19 severity with Omicron variant in South Africa, N. Engl. J. Med. 386 (14) (2022) 1314–1326.
[10] M.S. Mirtaleb, A.H. Mirtaleb, H. Nosrati, J. Heshmatnia, R. Falak, R.Z. Emameh, Potential therapeutic agents to COVID-19: an update review on antiviral therapy, immunotherapy, and cell therapy, Biomed. Pharmacother. 138 (2021), 111518.
[11] M. Gatti, F. De Ponti, Drug repurposing in the COVID-19 era: insights from case studies showing pharmaceutical peculiarities, Pharmaceutics 13 (2021) 302.
[12] A.M. Rabie, Potent toxic effects of Taroxaz-104 on the replication of SARS-CoV-2 particles, Chem. Biol. Interact. 343 (2021), 109480.
[13] A.M. Rabie, Cyanorona-20: the first potent anti-SARS-CoV-2 agent, Int. Immunopharm. 98 (2021), 107831.
[14] R. Singh, V.K. Bhardwaj, J. Sharma, R. Purohit, S. Kumar, In-silico evaluation of bioactive compounds from tea as potential SARS-CoV-2 nonstructural protein 16 inhibitors, J. Tradit., Complementary Med. 12 (2022) 35–43.
[15] J. Sharma, V.K. Bhardwaj, R. Singh, V. Rajendran, R. Purohit, S. Kumar, An in-silico evaluation of different bioactive molecules of tea for their inhibition potency against non structural protein-15 of SARS-CoV-2, Food Chem. 346 (2021), 128933.
[16] S. Zhang, K. Amahong, C. Zhang, F. Li, J. Gao, Y. Qiu, F. Zhu, RNA–RNA interactions between SARS-CoV-2 and host benefit viral development and evolution during COVID-19 infection, Briefings Bioinf. 23 (2022), bbab397.
[17] V.K. Bhardwaj, R. Singh, P. Das, R. Purohit, Evaluation of acridinedione analogs as potential SARS-CoV-2 main protease inhibitors and their comparison with repurposed anti-viral drugs, Comput. Biol. Med. 128 (2021), 104117.
[18] W.K. Chan, K.M. Olson, J.W. Wotring, J.Z. Sexton, H.A. Carlson, J.R. Traynor, In silico analysis of SARS-CoV-2 proteins as targets for clinically available drugs, Sci. Rep. 12 (2022) 1–12.
[19] S. Bharadwaj, S.A. El-Kafraway, T.A. Alandijany, L.H. Bajrai, A.A. Shah, A. Dubey, A.K. Sahoo, U. Yadava, M.A. Kamal, E.I. Azhar, Structure-Based identification of natural products as SARS-CoV-2 Mpro antagonist from Echinacea angustifolia using computational approaches, Viruses 13 (2021) 305.
[20] M.M. Ngwe Tun, K. Toume, E. Luvai, K.M. Nwe, S. Mizukami, K. Hirayama, K. Komatsu, K. Morita, The discovery of herbal drugs and natural compounds as inhibitors of SARS-CoV-2 infection in vitro, J. Nat. Med. (2022) 1–8.
[21] A.M. Rabie, Discovery of Taroxaz-104: the first potent antidote of SARS-CoV-2 VOC-202012/01 strain, J. Mol. Struct. 1246 (2021), 131106.
[22] L. Runfeng, H. Yunlong, H. Jicheng, P. Weiqi, M. Qinhai, S. Yongxia, L. Chufang, Z. Jin, J. Zhenhua, J. Haiming, Lianhuaqingwen exerts anti-viral and anti-inflammatory activity against novel coronavirus (SARS-CoV-2), Pharmacol. Res. 156 (2020), 104761.
[23] A.M. Rabie, New potential inhibitors of coronaviral main protease (CoV-Mpro): strychnine bush, pineapple, and ginger could be natural enemies of COVID-19, Int. J. Network. Commun. 9 (2022) 433–445.
[24] J.-T. Jan, T.-J.R. Cheng, Y.-P. Juang, H.-H. Ma, Y.-T. Wu, W.-B. Yang, C.-W. Cheng, X. Chen, T.-H. Chou, J.-J. Shie, Identification of existing pharmaceuticals and herbal medicines as inhibitors of SARS-CoV-2 infection, Proc. Natl. Acad. Sci. USA 118 (2021), e2021579118.
[25] P. Singh, S.S. Chauhan, S. Pandit, M. Sinha, S. Gupta, A. Gupta, R. Parthasarathi, The dual role of phytochemicals on SARS-CoV-2 inhibition by targeting host and viral proteins, J. Tradit., Complementary Med. 12 (2022) 90–99.
[26] D. Brian, R. Baric, Coronavirus genome structure and replication, Curr. Top. Microbiol. Immunol. 287 (2005) 1–30.
[27] M.Z. Tay, C.M. Poh, L. Rénia, P.A. MacAry, L.F. Ng, The trinity of COVID-19: immunity, inflammation and intervention, Nat. Rev. Immunol. 20 (2020) 363–374.
[28] K. Anand, G.J. Palm, J.R. Mesters, S.G. Siddell, J. Ziebuhr, R. Hilgenfeld, Structure of coronavirus main proteinase reveals combination of a chymotrypsin fold with an extra α-helical domain, EMBO J. 21 (2002) 3213–3224.
[29] H. Yang, M. Yang, Y. Ding, Y. Liu, Z. Lou, Z. Zhou, L. Sun, L. Mo, S. Ye, H. Pang, The crystal structures of severe acute respiratory syndrome virus main protease and its complex with an inhibitor, Proc. Natl. Acad. Sci. USA 100 (2003) 13190–13195.
[30] W. Rut, Z. Lv, M. Zmudzinski, S. Patchett, D. Nayak, S.J. Snipas, F. El Oualid, T. T. Huang, M. Bekes, M. Drag, Activity profiling and crystal structures of inhibitor-bound SARS-CoV-2 papain-like protease: a framework for anti–COVID-19 drug design, Sci. Adv. 6 (2020), eabd4596.
[31] E. Snijder, E. Decroly, J. Ziebuhr, The nonstructural proteins directing coronavirus RNA synthesis and processing, Adv. Virus Res. 96 (2016) 59–126.
[32] R. Ulferts, J. Ziebuhr, Nidovirus ribonucleases: structures and functions in viral replication, RNA Biol. 8 (2011) 295–304.
[33] J. Ziebuhr, E.J. Snijder, A.E. Gorbalenya, Virus-encoded proteinases and proteolytic processing in the Nidovirales, J. Gen. Virol. 81 (2000) 853–879.

[34] G. Sutton, E. Fry, L. Carter, S. Sainsbury, T. Walter, J. Nettleship, N. Berrow, R. Owens, R. Gilbert, A.J.S. Davidson, The nsp9 replicase protein of SARS-coronavirus, Struct. Funct. Insights 12 (2004) 341–353.

[35] D.R. Littler, B.S. Gully, R.N. Colson, J. Rossjohn, Crystal structure of the SARS-CoV-2 non-structural protein 9, Nsp9, iScience 23 (2020), 101258.

[36] Y. Chen, Q. Liu, D. Guo, Emerging coronaviruses: genome structure, replication, and pathogenesis, J. Med. Virol. 92 (2020) 418–423.

[37] T. Shu, M. Huang, D. Wu, Y. Ren, X. Zhang, Y. Han, J. Mu, R. Wang, Y. Qiu, D.-Y. Zhang, SARS-coronavirus-2 Nsp13 possesses NTPase and RNA helicase activities that can be inhibited by bismuth salts, Virol. Sin. 35 (2020) 321–329.

[38] Y. Chen, D. Guo, Molecular mechanisms of coronavirus RNA capping and methylation, Virol. Sin. 31 (2016) 3–11.

[39] P. Krafcikova, J. Silhan, R. Nencka, E. Boura, Structural analysis of the SARS-CoV-2 methyltransferase complex involved in RNA cap creation bound to sinefungin, Nat. Commun. 11 (2020) 1–7.

[40] Y. Peng, N. Du, Y. Lei, S. Dorje, J. Qi, T. Luo, G.F. Gao, H. Song, Structures of the SARS-CoV-2 nucleocapsid and their perspectives for drug design, EMBO J. 39 (2020), e105938.

[41] S.N. Lou, Y.C. Lai, Y.S. Hsu, C.T. Ho, Phenolic content, antioxidant activity and effective compounds of kumquat extracted by different solvents, Food Chem. 197 (2016) 1–6.

[42] G.C. Pamnani, P. Vardhan, R.K. Soni, Management approach to Covid-19 associated upper respiratory tract infection in Ayurveda: a review study, J. Ayurveda 14 (2020) 49.

[43] P.A. Jyothi, A. Dileep, D. Devarajan, A. Sharma, S. Kumari, S. Rathuri, S. Rai, P. Dharmarajan, T.M. Nesari, Three case reports of moderate COVID-19 infection managed through Ayurvedic approach, J. Ayurveda Case Rep 3 (2020) 84.

[44] K. Chambyal, S. Sharma, S. Sharma, Ayurveda prophylaxis and intervention for COVID-19 Pandemic, J. Ayurveda 14 (2020) 22.

[45] S. Kumar, Ayurveda interpretation, diagnostic, and probable management of COVID-19 pandemic, J. Ind. Sys. Med 8 (2020) 91.

[46] A.A. Panagiotopoulos, I. Karakasiliotis, D.M. Kotzampasi, M. Dimitriou, G. Sourvinos, M. Kampa, S. Pirintsos, E. Castanas, V. Daskalakis, Natural polyphenols inhibit the dimerization of the SARS-CoV-2 main protease: the case of fortunellin and its structural analogs, Molecules 26 (2021) 6068.

[47] H.X. Xu, M. Wan, H. Dong, P.P. But, L.Y. Foo, Inhibitory activity of flavonoids and tannins against HIV-1 protease, Biol. Pharm. Bull. 23 (2000) 1072–1076.

[48] W. Rizvi, M. Rizvi, R. Kumar, A. Kumar, I. Shukla, M. Parveen, Antibacterial activity of Ficus lyrata-An in vitro study, Int. J. Pharmacol. 8 (2010) 7.

[49] W. Xue, P. Wang, G. Tu, F. Yang, G. Zheng, X. Li, X. Li, Y. Chen, X. Yao, F. Zhu, Computational identification of the binding mechanism of a triple reuptake inhibitor amitifadine for the treatment of major depressive disorder, Phys. Chem. Chem. Phys. 20 (2018) 6606–6616.

[50] T. Fu, G. Zheng, G. Tu, F. Yang, Y. Chen, X. Yao, X. Li, W. Xue, F. Zhu, Exploring the binding mechanism of metabotropic glutamate receptor 5 negative allosteric modulators in clinical trials by molecular dynamics simulations, ACS Chem. Neurosci. 9 (2018) 1492–1502.

[51] A.M. Rabie, Potent inhibitory activities of the adenosine analogue cordycepin on SARS-CoV-2 replication, ACS Omega 7 (2022) 2960–2969.

[52] H.M. Berman, J. Westbrook, Z. Feng, G. Gilliland, T.N. Bhat, H. Weissig, I. N. Shindyalov, P.E. Bourne, The protein data bank, Nucleic Acids Res. 28 (2000) 235–242.

[53] E.F. Pettersen, T.D. Goddard, C.C. Huang, G.S. Couch, D.M. Greenblatt, E. C. Meng, T.E. Ferrin, UCSF Chimera—a visualization system for exploratory research and analysis, J. Comput. Chem. 25 (2004) 1605–1612.

[54] S. Kim, J. Chen, T. Cheng, A. Gindulyte, J. He, S. He, Q. Li, B.A. Shoemaker, P. A. Thiessen, B. Yu, PubChem 2019 update: improved access to chemical data, Nucleic Acids Res. 47 (2019) D1102–D1109.

[55] N.M. O`Boyle, M. Banck, C.A. James, C. Morley, T. Vandermeersch, G. R. Hutchison, Open Babel: an open chemical toolbox, J. Cheminf. 3 (2011) 1–14.

[56] J. Eberhardt, D. Santos-Martins, A.F. Tillack, S. Forli, AutoDock Vina 1.2. 0: new docking methods, expanded force field, and python bindings, J. Chem. Inf. Model. 61 (2021) 3891–3898.

[57] O. Trott, A.J. Olson, AutoDock Vina: improving the speed and accuracy of docking with a new scoring function, efficient optimization, and multithreading, J. Comput. Chem. 31 (2010) 455–461.

[58] A. Grosdidier, V. Zoete, O. Michielin, SwissDock, a protein-small molecule docking web service based on EADock DSS, Nucleic Acids Res. 39 (2011) W270–W277.

[59] M.J. Abraham, T. Murtola, R. Schulz, S. Páll, J.C. Smith, B. Hess, E. Lindahl, GROMACS: high performance molecular simulations through multi-level parallelism from laptops to supercomputers, Software 1 (2015) 19–25.

[60] J. Huang, S. Rauscher, G. Nawrocki, T. Ran, M. Feig, B.L. de Groot, H. Grubmuller, A.D. MacKerell Jr., CHARMM36m: an improved force field for folded and intrinsically disordered proteins, Nat. Methods 14 (2017) 71–73.

[61] V. Zoete, M.A. Cuendet, A. Grosdidier, O. Michielin, SwissParam: a fast force field generation tool for small organic molecules, J. Comput. Chem. 32 (2011) 2359–2368.

[62] T. Darden, D. York, L. Pedersen, Particle mesh Ewald: an N· log (N) method for Ewald sums in large systems, J. Chem. Phys. 98 (1993) 10089–10092.

[63] B. Hess, H. Bekker, H.J. Berendsen, J.G. Fraaije, LINCS: a linear constraint solver for molecular simulations, J. Comput. Chem. 18 (1997) 1463–1472.

[64] G. Bussi, D. Donadio, M. Parrinello, Canonical sampling through velocity rescaling, J. Chem. Phys. 126 (2007), 014101.

[65] M. Parrinello, A. Rahman, Polymorphic transitions in single crystals: a new molecular dynamics method, J. Appl. Phys. 52 (1981) 7182–7190.

[66] W.F. Van Gunsteren, H.J. Berendsen, A leap-frog algorithm for stochastic dynamics, Mol. Simulat. 1 (1988) 173–185.

[67] P. Turner, XMGRACE, 5.1. 19, Center For Coastal Land-Margin Research, Oregon Graduate Institute of Science Technology, Beaverton, 2005.

[68] D.A. Case, H.M. Aktulga, K. Belfon, I. Ben-Shalom, S.R. Brozell, D. Cerutti, T. Cheatham, V.W.D. Cruzeiro, T. Darden, R.E. Duke, Amber 2021: Reference Manual, 2021.

[69] M.S. Valdés-Tresanco, M.E. Valdés-Tresanco, P.A. Valiente, E. Moreno, gmx_MMPBSA: a new tool to perform end-state free energy calculations with GROMACS, J. Chem. Theor. Comput. 17 (2021) 6281–6291.

[70] B.R. Miller III, T.D. McGee Jr., J.M. Swails, N. Homeyer, H. Gohlke, A.E. Roitberg, MMPBSA. py: an efficient program for end-state free energy calculations, J. Chem. Theor. Comput. 8 (2012) 3314–3321.

[71] W. Humphrey, A. Dalke, K. Schulten, VMD: visual molecular dynamics, J. Mol. Graph. 14 (1996) 33–38.

[72] G. Xiong, Z. Wu, J. Yi, L. Fu, Z. Yang, C. Hsieh, M. Yin, X. Zeng, C. Wu, A. Lu, ADMETlab 2.0: an integrated online platform for accurate and comprehensive predictions of ADMET properties, Nucleic Acids Res. 49 (2021). W5-W14.

[73] D.E. Pires, T.L. Blundell, D.B. Ascher, pkCSM: predicting small-molecule pharmacokinetic and toxicity properties using graph-based signatures, J. Med. Chem. 58 (2015) 4066–4072.

[74] M.J. Keiser, B.L. Roth, B.N. Armbruster, P. Ernsberger, J.J. Irwin, B.K. Shoichet, Relating protein pharmacology by ligand chemistry, Nat. Biotechnol. 25 (2007) 197–206.

[75] D. Gfeller, A. Grosdidier, M. Wirth, A. Daina, O. Michielin, V. Zoete, SwissTargetPrediction: a web server for target prediction of bioactive small molecules, Nucleic Acids Res. 42 (2014) W32–W38.

[76] M.V. Kuleshov, M.R. Jones, A.D. Rouillard, N.F. Fernandez, Q. Duan, Z. Wang, S. Koplev, S.L. Jenkins, K.M. Jagodnik, A. Lachmann, M.G. McDermott, C. D. Monteiro, G.W. Gundersen, A. Ma'ayan, Enrichr: a comprehensive gene set enrichment analysis web server 2016 update, Nucleic Acids Res. 44 (2016) W90–W97.

[77] H. Wickham, Data Analysis, Ggplot2, Springer, 2016, pp. 189–201.

[78] N.T. Doncheva, J.H. Morris, J. Gorodkin, L.J. Jensen, Cytoscape StringApp: network analysis and visualization of proteomics data, J. Proteome Res. 18 (2019) 623–632.

[79] C.-H. Chin, S.-H. Chen, H.-H. Wu, C.-W. Ho, M.-T. Ko, C.-Y. Lin, cytoHubba: identifying hub objects and sub-networks from complex interactome, BMC Syst. Biol. 8 (4) (2014) 1–7.

[80] M. Kanehisa, S. Goto, KEGG: kyoto encyclopedia of genes and genomes, Nucleic Acids Res. 28 (2000) 27–30.

[81] D.W. Kneller, G. Phillips, H.M. O'Neill, R. Jedrzejczak, L. Stols, P. Langan, A. Joachimiak, L. Coates, A. Kovalevsky, Structural plasticity of SARS-CoV-2 3CL M pro active site cavity revealed by room temperature X-ray crystallography, Nat. Commun. 11 (2020) 1–6.

[82] K. Świderek, V. Moliner, Revealing the molecular mechanisms of proteolysis of SARS-CoV-2 M pro by QM/MM computational methods, Chem. Sci. 11 (2020) 10626–10630.

[83] D.R. Littler, B.S. Gully, R.N. Colson, J. Rossjohn, Crystal structure of the SARS-CoV-2 non-structural protein 9, Nsp9, iScience (2020) 23.

[84] E. Callaway, Heavily mutated Omicron variant puts scientists on alert, Nature 600 (2021) 21.

[85] Y.L. Ng, C.K. Salim, J.J.H. Chu, Drug repurposing for COVID-19: approaches, challenges and promising candidates, Pharmacol. Ther. 228 (2021), 107930.

[86] S. Poudel, A. Ishak, J. Perez-Fernandez, E. Garcia, D.A. León-Figueroa, L. Romaní, D.K. Bonilla-Aldana, A.J. Rodriguez-Morales, Highly mutated SARS-CoV-2 Omicron variant sparks significant concern among global experts–What is known so far? Trav. Med. Infect. Dis. 45 (2022), 102234.

[87] A.M. Rabie, Two antioxidant 2, 5-disubstituted-1, 3, 4-oxadiazoles (CoViTris2020 and ChloViD2020): successful repurposing against COVID-19 as the first potent multitarget anti-SARS-CoV-2 drugs, New J. Chem. 45 (2021) 761–771.

[88] A.M. Rabie, CoViTris2020 and ChloViD2020: a striking new hope in COVID-19 therapy, Mol. Divers. 25 (2021) 1839–1854.

[89] C. Zhao, Y. Zhang, H. Liu, P. Li, H. Zhang, G. Cheng, Fortunellin protects against high fructose-induced diabetic heart injury in mice by suppressing inflammation and oxidative stress via AMPK/Nrf-2 pathway regulation, Biochem. Biophys. Res. Commun. 490 (2017) 552–559.

[90] Y. Xiong, J. Qiu, C. Li, Y. Qiu, L. Guo, Y. Liu, J. Wan, Y. Li, G. Wu, L. Wang, Z. Zhou, J. Dong, C. Du, D. Chen, H. Guo, Fortunellin-Induced modulation of phosphatase and tensin homolog by MicroRNA-374a decreases inflammation and maintains intestinal barrier function in colitis, Front. Immunol. 9 (2018) 83.

[91] S. Genheden, U. Ryde, The MM/PBSA and MM/GBSA methods to estimate ligand-binding affinities, Expet Opin. Drug Discov. 10 (2015) 449–461.

[92] Y.L. Weng, S.R. Naik, N. Dingelstad, M.R. Lugo, S. Kalyaanamoorthy, A. Ganesan, Molecular dynamics and in silico mutagenesis on the reversible inhibitor-bound SARS-CoV-2 main protease complexes reveal the role of lateral pocket in enhancing the ligand affinity, Sci. Rep. 11 (2021) 7429.

[93] T.S. Komatsu, N. Okimoto, Y.M. Koyama, Y. Hirano, G. Morimoto, Y. Ohno, M. Taiji, Drug binding dynamics of the dimeric SARS-CoV-2 main protease, determined by molecular dynamics simulation, Sci. Rep. 10 (2020), 16986.

[94] A. Shitrit, D. Zaidman, O. Kalid, I. Bloch, D. Doron, T. Yarnizky, I. Buch, I. Segev, E. Ben-Zeev, E. Segev, Conserved interactions required for inhibition of the main protease of severe acute respiratory syndrome coronavirus 2 (SARS-CoV-2), Sci. Rep. 10 (2020) 1–11.

[95] W. Rut, Z. Lv, M. Zmudzinski, S. Patchett, D. Nayak, S.J. Snipas, F. El Oualid, T. T. Huang, M. Bekes, M. Drag, Activity profiling and crystal structures of inhibitor-

bound SARS-CoV-2 papain-like protease: a framework for anti–COVID-19 drug design, J Science advances 6 (2020), eabd4596.

[96] E. De Wit, F. Feldmann, J. Cronin, R. Jordan, A. Okumura, T. Thomas, D. Scott, T. Cihlar, H. Feldmann, Prophylactic and therapeutic remdesivir (GS-5734) treatment in the rhesus macaque model of MERS-CoV infection, J Proceedings of the National Academy of Sciences 117 (2020) 6771–6776.

[97] G. Li, E. De Clercq, Therapeutic options for the 2019 novel coronavirus (2019-nCoV), J. Nat. Rev. Drug Discov. 19 (2020) 149–150.

[98] T.P. Sheahan, A.C. Sims, S.R. Leist, A. Schäfer, J. Won, A.J. Brown, S. A. Montgomery, A. Hogg, D. Babusis, M.O. Clarke, Comparative therapeutic efficacy of remdesivir and combination lopinavir, ritonavir, and interferon beta against MERS-CoV, J. Nat. Commun. 11 (2020) 1–14.

[99] R.H. Pirzada, M. Haseeb, M. Batool, M. Kim, S. Choi, Remdesivir and ledipasvir among the FDA-approved antiviral drugs have potential to inhibit SARS-CoV-2 replication, J. Cell. 10 (2021) 1052.

[100] Y. Kim, J. Wower, N. Maltseva, C. Chang, R. Jedrzejczak, M. Wilamowski, S. Kang, V. Nicolaescu, G. Randall, K. Michalska, Tipiracil binds to uridine site and inhibits Nsp15 endoribonuclease NendoU from SARS-CoV-2, J Communications biology 4 (2021) 1–11.

[101] M.C. Pillon, M.N. Frazier, L.B. Dillard, J.G. Williams, S. Kocaman, J.M. Krahn, L. Perera, C.K. Hayne, J. Gordon, Z.D. Stewart, Cryo-EM structures of the SARS-CoV-2 endoribonuclease Nsp15 reveal insight into nuclease specificity and dynamics, J. Nat. Commun. 12 (2021) 1–12.

[102] A.B. Farias, G. Candiotto, L. Siragusa, L. Goracci, G. Cruciani, E.R. Oliveira, B. A. Horta, Targeting Nsp9 as an anti-SARS-CoV-2 strategy, New J. Chem. 45 (2021) 522–525.

[103] R. Ponnusamy, R. Moll, T. Weimar, J.R. Mesters, R. Hilgenfeld, Variable oligomerization modes in coronavirus non-structural protein 9, J. Mol. Biol. 383 (2008) 1081–1096.

[104] D.R. Littler, M. Liu, J.L. McAuley, S.A. Lowery, P.T. Illing, B.S. Gully, A. W. Purcell, I.R. Chandrashekaran, S. Perlman, D.F. Purcell, A natural product compound inhibits coronaviral replication in vitro by binding to the conserved Nsp9 SARS-CoV-2 protein, J. Biol. Chem. 297 (2021).

[105] M. Liu, D.R. Littler, J. Rossjohn, R.J. Quinn, Binding studies of the prodrug HAO472 to SARS-Cov-2 Nsp9 and variants, J ACS omega 7 (2022) 7327–7332.

[106] R. Vivek-Ananth, S. Krishnaswamy, A. Samal, Potential phytochemical inhibitors of SARS-CoV-2 helicase Nsp13: a molecular docking and dynamic simulation study, J Molecular diversity 26 (2022) 429–442.

[107] E. Pitsillou, J. Liang, A. Hung, T.C. Karagiannis, Modelling, the SARS-CoV-2 helicase as a target for antiviral therapy: identification of potential small molecule inhibitors by in silico modelling, J. Mol. Graph. 114 (2022), 108193.

[108] C. Al Khoury, Z. Bashir, S. Tokajian, N. Nemer, G. Merhi, G. Nemer, medicine, in silico evidence of beauvericin antiviral activity against SARS-CoV-2, J. Comp. Biol. 141 (2022), 105171.

[109] G.R. Perez-Lemus, C.A. Menéndez, W. Alvarado, F. Byléhn, J.J. de Pablo, Toward wide-spectrum antivirals against coronaviruses: molecular characterization of SARS-CoV-2 NSP13 helicase inhibitors, J Science advances 8 (2022), eabj4526.

[110] M.A. White, W. Lin, X. Cheng, Discovery of COVID-19 inhibitors targeting the SARS-CoV-2 Nsp13 helicase, J. Phys. Chem. Lett. 11 (2020) 9144–9151.

[111] M.A. El Hassab, W.M. Eldehna, S.T. Al-Rashood, A. Alharbi, R.O. Eskandrani, H. M. Alkahtani, E.B. Elkaeed, S.M. Abou-Seri, Multi-stage structure-based virtual screening approach towards identification of potential SARS-CoV-2 NSP13 helicase inhibitors, J. Enzym. Inhib. Med. Chem. 37 (2022) 563–572.

[112] T. Viswanathan, S. Arya, S.-H. Chan, S. Qi, N. Dai, A. Misra, J.-G. Park, F. Oladunni, D. Kovalskyy, R.A. Hromas, Structural basis of RNA cap modification by SARS-CoV-2, J. Nat. Commun. 11 (2020) 1–7.

[113] L.-J. Chang, T.-H. Chen, NSP16 2′-O-MTase in coronavirus pathogenesis: possible prevention and treatments strategies, J Viruses 13 (2021) 538.

[114] M. Rosas-Lemus, G. Minasov, L. Shuvalova, N.L. Inniss, O. Kiryukhina, J. Brunzelle, K.J. Satchell, High-resolution structures of the SARS-CoV-2 2′-O-methyltransferase reveal strategies for structure-based inhibitor design, J Science signaling 13 (2020), eabe1202.

[115] J. Liang, E. Pitsillou, L. Burbury, A. Hung, T.C. Karagiannis, In silico investigation of potential small molecule inhibitors of the SARS-CoV-2 nsp10-nsp16 methyltransferase complex, J Chemical Physics Letters 774 (2021), 138618.

[116] E. Tazikeh-Lemeski, S. Moradi, R. Raoufi, M. Shahlaei, M.A.M. Janlou, S. Zolghadri, Targeting SARS-COV-2 non-structural protein 16: a virtual drug repurposing study, J. Biomol. Struct. Dyn. 39 (2021) 4633–4646.

[117] S. Kang, M. Yang, Z. Hong, L. Zhang, Z. Huang, X. Chen, S. He, Z. Zhou, Z. Zhou, Q. Chen, Crystal structure of SARS-CoV-2 nucleocapsid protein RNA binding domain reveals potential unique drug targeting sites, Acta Pharm. Sin. B 10 (2020) 1228–1238.

[118] M.T. Khan, M.T. Zeb, H. Ahsan, A. Ahmed, A. Ali, K. Akhtar, S.I. Malik, Z. Cui, S. Ali, A.S. Khan, SARS-CoV-2 nucleocapsid and Nsp3 binding: an in silico study, Arch. Microbiol. 203 (2021) 59–66.

[119] O. Terrier, S. Dilly, A. Pizzorno, D. Chalupska, J. Humpolickova, E. Bouřa, F. Berenbaum, S. Quideau, B. Lina, B. Fève, Antiviral properties of the NSAID drug naproxen targeting the nucleoprotein of SARS-CoV-2 coronavirus, Molecules 26 (2021) 2593.

[120] J.-N. Hsu, J.-S. Chen, S.-M. Lin, J.-Y. Hong, Y.-J. Chen, U.-S. Jeng, S.-Y. Luo, M.-H. Hou, Targeting the N-terminus domain of the coronavirus nucleocapsid protein induces abnormal oligomerization via allosteric modulation, Front. Mol. Biosci. 9 (2022).

[121] Y.-T. Wang, X.-Y. Long, X. Ding, S.-R. Fan, J.-Y. Cai, B.-J. Yang, X.-F. Zhang, R.-h. Luo, L. Yang, T. Ruan, Novel nucleocapsid protein-targeting phenanthridine inhibitors of SARS-CoV-2, Eur. J. Med. Chem. 227 (2022), 113966.

[122] G. Minasov, L. Shuvalova, G. Wiersum, K. Satchell, 2.05 Angstrom Resolution Crystal Structure of C-Terminal Dimerization Domain of Nucleocapsid Phosphoprotein from SARS-CoV-2. 2020, Center for Structural Genomics of Infectious Diseases (CSGID)), 2020, https://doi.org/10.2210/pdb6wji/pdb.

[123] A. Panagiotopoulos, M. Tseliou, I. Karakasiliotis, D.M. Kotzampasi, V. Daskalakis, N. Kesesidis, G. Notas, C. Lionis, M. Kampa, S. Pirintsos, p-cymene impairs SARS-CoV-2 and Influenza A (H1N1) viral replication: in silico predicted interaction with SARS-CoV-2 nucleocapsid protein and H1N1 nucleoprotein, Pharmacology research & perspectives 9 (2021), e00798.

[124] J. Rani, A. Bhargav, F.I. Khan, S. Ramachandran, D. Lai, U. Bajpai, In silico prediction of natural compounds as potential multi-target inhibitors of structural proteins of SARS-CoV-2, J. Biomol. Struct. Dyn. (2021) 1–17.

[125] M. Zhao, Y. Yu, L.-M. Sun, J.-Q. Xing, T. Li, Y. Zhu, M. Wang, Y. Yu, W. Xue, T. Xia, GCG inhibits SARS-CoV-2 replication by disrupting the liquid phase condensation of its nucleocapsid protein, Nat. Commun. 12 (2021) 1–14.

[126] J.-L. Darlix, H. de Rocquigny, O. Mauffret, Y. Mély, Retrospective on the all-in-one retroviral nucleocapsid protein, Virus Res. 193 (2014) 2–15.

[127] E. Mortaz, P. Tabarsi, H. Jamaati, N. Dalil Roofchayee, N.K. Dezfuli, S. M. Hashemian, A. Moniri, M. Marjani, M. Malekmohammad, D. Mansouri, Increased serum levels of soluble TNF-α receptor is associated with ICU mortality in COVID-19 patients, Front. Immunol. (2021) 1321.

[128] D.M. Del Valle, S. Kim-Schulze, H.H. Huang, N.D. Beckmann, S. Nirenberg, B. Wang, Y. Lavin, T.H. Swartz, D. Madduri, A. Stock, T.U. Marron, H. Xie, M. Patel, K. Tuballes, O. Van Oekelen, A. Rahman, P. Kovatch, J.A. Aberg, E. Schadt, S. Jagannath, M. Mazumdar, A.W. Charney, A. Firpo-Betancourt, D. R. Mendu, J. Jhang, D. Reich, K. Sigel, C. Cordon-Cardo, M. Feldmann, S. Parekh, M. Merad, S. Gnjatic, An inflammatory cytokine signature predicts COVID-19 severity and survival, Nat. Med. 26 (2020) 1636–1643.

[129] M. Letko, A. Marzi, V. Munster, Functional assessment of cell entry and receptor usage for SARS-CoV-2 and other lineage B betacoronaviruses, Nat Microbiol 5 (2020) 562–569.

[130] T.S. Rodrigues, K.S.G. de Sa, A.Y. Ishimoto, A. Becerra, S. Oliveira, L. Almeida, A. V. Goncalves, D.B. Perucello, W.A. Andrade, R. Castro, F.P. Veras, J.E. Toller-Kawahisa, D.C. Nascimento, M.H.F. de Lima, C.M.S. Silva, D.B. Caetite, R. B. Martins, I.A. Castro, M.C. Pontelli, F.C. de Barros, N.B. do Amaral, M. C. Giannini, L.P. Bonjorno, M.I.F. Lopes, R.C. Santana, F.C. Vilar, M. Auxiliadora-Martins, R. Luppino-Assad, S.C.L. de Almeida, F.R. de Oliveira, S.S. Batah, L. Siyuan, M.N. Benatti, T.M. Cunha, J.C. Alves-Filho, F.Q. Cunha, L.D. Cunha, F. G. Frantz, T. Kohlsdorf, A.T. Fabro, E. Arruda, R.D.R. de Oliveira, P. Louzada-Junior, D.S. Zamboni, Inflammasomes are activated in response to SARS-CoV-2 infection and are associated with COVID-19 severity in patients, J. Exp. Med. 218 (2021).

[131] A.L. Horenstein, A.C. Faini, F. Malavasi, CD38 in the age of COVID-19: a medical perspective, Physiol. Rev. 101 (2021) 1457–1486.

[132] M.L. Yeung, Y. Yao, L. Jia, J.F. Chan, K.H. Chan, K.F. Cheung, H. Chen, V.K. Poon, A.K. Tsang, K.K. To, M.K. Yiu, J.L. Teng, H. Chu, J. Zhou, Q. Zhang, W. Deng, S. K. Lau, J.Y. Lau, P.C. Woo, T.M. Chan, S. Yung, B.J. Zheng, D.Y. Jin, P. W. Mathieson, C. Qin, K.Y. Yuen, MERS coronavirus induces apoptosis in kidney and lung by upregulating Smad7 and FGF2, Nat Microbiol 1 (2016), 16004.

[133] S. Meini, T. Giani, C. Tascini, Intussusceptive angiogenesis in Covid-19: hypothesis on the significance and focus on the possible role of FGF2, Mol. Biol. Rep. 47 (2020) 8301–8304.

[134] A.N. El-Din, K.A.E.-S. Ata, A.R. Abdel-Gawad, N.F. Fahmy, Impact of high serum levels of MMP-7, MMP-9, TGF-β and PDGF macrophage activation markers on severity of COVID-19 in obese-diabetic patients, Infect. Drug Resist. 14 (2021) 4015.

[135] A.S.M. Moin, T. Sathyapalan, S.L. Atkin, A.E. Butler, Pro-fibrotic M2 macrophage markers may increase the risk for COVID19 in type 2 diabetes with obesity, Metab. Clin. Exp. 112 (2020).

[136] F. Syed, W. Li, R.F. Relich, P.M. Russell, S. Zhang, M.K. Zimmerman, Q. Yu, Excessive matrix metalloproteinase-1 and hyperactivation of endothelial cells occurred in COVID-19 patients and were associated with the severity of COVID-19, J. Infect. Dis. 224 (1) (2021) 60–69.

[137] M. McMahon, S. Ye, J. Pedrina, D. Dlugolenski, J. Stambas, Extracellular matrix enzymes and immune cell biology, Front. Mol. Biosci. 8 (2021), 703868.

[138] P. Prasher, M. Sharma, R. Gunupuru, Targeting cyclooxygenase enzyme for the adjuvant COVID-19 therapy, Drug Dev. Res. 82 (2021) 469–473.

[139] M. Raaben, A.W. Einerhand, L.J. Taminiau, M. Van Houdt, J. Bouma, R. H. Raatgeep, H.A. Büller, C.A. De Haan, J.W. Rossen, Cyclooxygenase activity is important for efficient replication of mouse hepatitis virus at an early stage of infection, Virol. J. 4 (2007) 1–5.